Chapter 2
A Generalized Force-Modified Potential Energy Surface (G-FMPES) for Mechanochemical Simulations

Sanjiv K. Jha and Gopinath Subramanian

Abstract We describe the modifications that a spatially varying external force produces on a Born-Oppenheimer potential energy surface (PES), and in this chapter, we present a formulation for describing a Generalized Force-Modified Potential Energy Surface (G-FMPES). Our formulation shows that the spatially varying force resembling hydrostatic pressure results in the G-FMPES having curvature different from that of the unmodified PES. Using electronic structure methods, the effect of pseudo-hydrostatic pressure on the PES is exemplified by calculating atomistic quantities (including transition states) for (i) conformational transitions in ethane (C_2H_6) and RDX (hexahydro-1,3,5-trinitro-*s*-triazine) molecules, (ii) the decomposition of RDX, and (iii) a Diels-Alder reaction between 1,3-butadiene and ethylene. The calculated transition states and Hessian matrices of stationary points of ethane and RDX molecules show that spatially varying external forces shift the stationary points and modify the curvature of the PES, thereby affecting the harmonic transition rates by altering both the energy barrier as well as the prefactor. The harmonic spectra of both molecules are blue-shifted with increasing compressive "pressure." Some stationary points on the RDX-PES disappear under the application of the external force, indicating the merging of an energy minimum with a saddle point. This change in the topology of the PES demonstrates that new reaction pathways may be introduced by the application of mechanical forces. Part of this chapter is reproduced with permission from Refs. (J Chem Phys 143(13):134109 [1]) Copyright 2015 AIP Publishing, (J Chem Phys 145(7):074307 [2]) Copyright 2016 AIP Publishing, and (Int J Quantum Chem 117(20):e25426 [3]) Copyright 2017 John Wiley & Sons.

S. K. Jha
Mathematics and Science Department, GateWay Community College, Maricopa Community Colleges, 108 N 40th Street, Phoenix, AZ 85034, USA
e-mail: sanjiv.jha@gatewaycc.edu

G. Subramanian (✉)
X-Computational Physics Division, Los Alamos National Laboratory, Los Alamos, NM 87545, USA
e-mail: gss@lanl.gov

M. Shukla et al. (eds.), *Emerging Materials and Environment*,
Challenges and Advances in Computational Chemistry and Physics 37,
https://doi.org/10.1007/978-3-031-39470-6_2

2.1 Introduction

Since the early days of humanity, mechanochemistry has been used to accelerate chemical reactions. The earliest example is very likely the striking of two pieces of stone in order to produce fire. In more recent times, mechanochemistry has been recognized as the use of mechanical forces to modify the potential energy surface of a system, and consequently, modify reaction pathways and rates. Recently, there has been a resurgence of interest in examining systems that have a subset of their atoms subjected to an external force. Examples include computing activation energies for defect diffusion in the vicinity of dislocations [4, 5], ring opening of cyclobutene [6], the design of mechanophores [7], inducing forbidden reactions by violating the Woodward-Hoffman rules [8], exploring the energy landscapes of mechanosensitive molecules [9], and mechanophore activation [10–12].

Compressive hydrostatic pressures are another practically useful control variable, and it has long been known that reactions conducted at pressures different from atmospheric can have mechanisms and rates different from their counterparts at atmospheric pressure [13–16]. Examples include developing superconducting behavior in condensed rare gases, and ionic compounds [17], polymorphic crystal-crystal phase transition in aluminum phosphate (berlinite) [18], bacterial spore inactivation [19], and the oxidation of hydrogen [20]. On the atomic level, compressive hydrostatic pressure manifests itself as an external force on the atoms that are participating in a reaction and can therefore be considered a subset of mechanochemistry [1, 6, 8, 12, 21–28].

There are numerous ways to compress a molecule in a simulation. The majority of studies to date assume, for simplicity, that the external force applied to the atoms is constant [6, 21, 23, 25], but, this need not always be the case. One example of a spatially varying force is seen in problems relevant to irradiation damage where the transition rates of defects (such as single interstitials) in metals and oxides have been demonstrated to be a function of the macroscopic stress [29–32]. In these cases, defects are embedded in a uniform stress field, but the transmission of the macroscopically uniform stress to the atomic level almost inevitably results in the individual atoms experiencing a force that is a complex function of the current atomic configuration. Consequently, atoms involved in a transition will experience an external force that is a complex function of the reaction progress. Another example of a spatially varying force is seen in energetic materials such as RDX in either the presence of a macroscopic stress field [33–35], or in the vicinity of defects [36–40]. Here, as with the case of irradiation damage, the force on the atoms involved in a transition is a function of their position within the crystal. A third example is seen in molecules embedded in a non-uniform external field (e.g., as seen in ion traps [41] where the confining external potential is quadratic) which results in a force that is non-uniform throughout the molecule, and therefore, the assumption of a constant force can be a poor approximation. A fourth example is seen in single-molecule force spectroscopy [42, 43] where the constant force assumption is valid only in the limit of "soft" handles through which the force is transmitted to the molecule. Therefore, a more

realistic description of single-molecule pulling would also involve forces that are not constant.

The effects of external forces were recently investigated for several different systems [6–8, 23, 25, 27, 28]. Moreover, recent reviews were also published on the topic of mechanochemistry [22, 44, 45]. The effect of any external force (either constant or spatially varying) on a subset of atoms serves to modify the potential energy surface (PES) of the system being studied, and in this chapter, we present a formulation for describing a Generalized Force-Modified Potential Energy Surface (G-FMPES) [1]. This formulation can be used for both constant as well as spatially varying forces, and can be viewed as a generalization of earlier work by Ong et al. [6]. This formulation also shows that spatially varying forces result in the G-FMPES having a curvature different from that of the unmodified PES: this curvature change can be particularly important for studies that explore the G-FMPES by numerical integration [9], where the tacit assumption of unchanging curvatures is made. With the formulation of the G-FMPES in place, we show that standard atomistic techniques can be used to calculate quantities of practical interest, such as transition states and vibration spectra, under the influence of a spatially varying external force. We also discuss some results obtained for one particular mode of external load, which we refer to as pseudo-hydrostatic pressure, for conformation transitions in ethane (C_2H_6) and hexahydro-1,3,5-trinitro-*s*-triazine (RDX) [1], the decomposition of RDX [3], and a Diels-Alder reaction [2].

2.2 Methods

2.2.1 The Generalized Force-Modified Potential Energy Surface (G-FMPES)

Consider a 3-dimensional system comprised of N atoms with positions of all the atoms given by the $3N$-dimensional vector $\mathbf{R}$. Let the functional $V(\mathbf{R})$ denote the unmodified PES. We assume that the PES is smooth, and that third derivatives exist at all points. As is standard, the force on all the atoms is given by the negative gradient of the potential energy functional as

$$\mathbf{F}_{\text{grad}}(\mathbf{R}) = -\nabla V(\mathbf{R}) \tag{2.1}$$

In mechanochemical simulations, the external force, denoted by the $3N$-dimensional vector $\mathbf{F}_{\text{ext}}(\mathbf{R})$, is the result of an external potential $V_{\text{ext}}(\mathbf{R})$. These last two quantities are related by

$$\mathbf{F}_{\text{ext}}(\mathbf{R}) = -\nabla V_{\text{ext}}(\mathbf{R}) \tag{2.2}$$

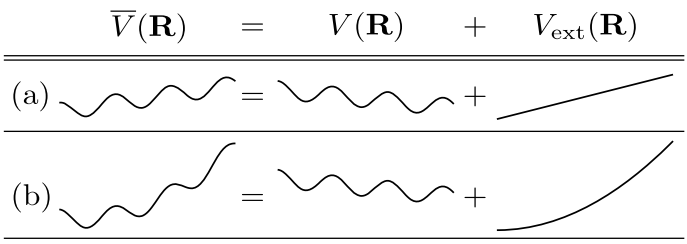

Fig. 2.1 A 1-dimensional generalized force-modified potential energy surface (G-FMPES), $\overline{V}(\mathbf{R})$, as the sum of an unmodified PES and an external potential. The schematic shows the results of adding two different kinds of external potentials: **a** linear, corresponding to a constant external force that preserves the curvature of the unmodified PES, and **b** quadratic, corresponding to a spatially varying force that changes the curvature of the unmodified PES. Reprinted (adapted) from [1], with the permission of AIP publishing

This external force, (form unspecified), modifies the PES and results in a G-FMPES:

$$\overline{V}(\mathbf{R}) = V(\mathbf{R}) + V_{\text{ext}}(\mathbf{R}) \tag{2.3}$$

This addition of functionals for a 1-dimensional PES is shown schematically in Fig. 2.1 for (a) linear, and (b) quadratic external potentials. We adopt the convention that a variable with an overline refers to a quantity computed on a G-FMPES. In mechanochemical simulations, the unmodified PES and external forces are prescribed, making it necessary to calculate the numerical value of $V_{\text{ext}}(\mathbf{R})$. As long as $\mathbf{F}_{\text{ext}}(\mathbf{R})$ is a conservative field, this is achieved by performing a path integral from a suitable reference configuration, say $\mathbf{R}_{\text{ref}}$, to the desired configuration $\mathbf{R}$ as

$$V_{\text{ext}}(\mathbf{R}) - V_{\text{ext}}(\mathbf{R}_{\text{ref}}) = \int_{\mathbf{s}=\mathbf{R}_{\text{ref}}}^{\mathbf{s}=\mathbf{R}} -\mathbf{F}_{\text{ext}}(\mathbf{s}) \cdot \mathrm{d}\mathbf{s} \tag{2.4}$$

$$= \int_{\mathbf{s}=\mathbf{R}}^{\mathbf{s}=\mathbf{R}_{\text{ref}}} \mathbf{F}_{\text{ext}}(\mathbf{s}) \cdot \mathrm{d}\mathbf{s} \tag{2.5}$$

Note that in the second integral, the integration path has been reversed by removing the negative sign. The actual path is unimportant (because of the conservative force field), and a straight line is chosen as it is possibly the simplest path. In most simulations, we are interested in the *relative* heights of stationary points, and therefore set $V_{\text{ext}}(\mathbf{R}_{\text{ref}}) = 0$. Equation (2.3) becomes

$$\overline{V}(\mathbf{R}) = V(\mathbf{R}) + \int_{\mathbf{s}=\mathbf{R}}^{\mathbf{s}=\mathbf{R}_{\text{ref}}} \mathbf{F}_{\text{ext}}(\mathbf{s}) \cdot \mathrm{d}\mathbf{s} \tag{2.6}$$

and shows that external forces can, in general, produce stationary points that are different from those on the unmodified PES.

As discussed in the introduction, the external force vector is not necessarily a constant. However, if we set $\mathbf{F}_{\text{ext}}$ to be a constant, as has been the case with many mechanochemical studies [6–12], Eq. (2.6) for the G-FMPES reduces to

$$\overline{V}(\mathbf{R}) = V(\mathbf{R}) + \mathbf{F}_{\text{ext}} \cdot (\mathbf{R}_{\text{ref}} - \mathbf{R}), \tag{2.7}$$

equivalent to the expression employed by previous studies. Thus, if we make the simplifying assumptions that previous researchers have made, our more general expression for the G-FMPES (Equation (2.6)) reduces to the simpler form employed in the past (Equation (2.7)).

2.2.2 Curvature of the G-FMPES

The local curvature of the G-FMPES is given by the Hessian matrix, which is in turn defined as the Jacobian of the gradient of the potential energy functional. Denoting the Hessian for the G-FMPES by $\overline{\mathbf{H}}(\mathbf{R})$, and applying the definition of the Hessian to the definition of a G-FMPES (Equation (2.3)), we obtain

$$\begin{aligned}\overline{\mathbf{H}}(\mathbf{R}) &= \mathbf{J}\left[\nabla \overline{V}(\mathbf{R})\right] \\ &= \mathbf{J}\left[\nabla \left\{V(\mathbf{R}) + V_{\text{ext}}(\mathbf{R})\right\}\right]\end{aligned} \tag{2.8}$$

Since the Jacobian and gradient operators are distributive, we get an expression for the Hessian matrix on the G-FMPES as

$$\begin{aligned}\overline{\mathbf{H}}(\mathbf{R}) &= \mathbf{H}(\mathbf{R}) - \mathbf{J}\left[\mathbf{F}_{\text{ext}}(\mathbf{R})\right] \\ &= \mathbf{H}(\mathbf{R}) + \mathbf{H}_{\text{ext}}(\mathbf{R})\end{aligned} \tag{2.9}$$

where $\mathbf{H}(\mathbf{R})$ is the Hessian matrix of the unmodified PES, and we have designated

$$\mathbf{H}_{\text{ext}}(\mathbf{R}) = -\mathbf{J}\left[\mathbf{F}_{\text{ext}}(\mathbf{R})\right] \tag{2.10}$$

Equations (2.9) and (2.10) show that if the external force $\mathbf{F}_{\text{ext}}$ is a constant, then $\mathbf{H}_{\text{ext}}(\mathbf{R}) = 0$, the Hessian is unchanged, and the two surfaces have the same curvature (as shown in Fig. 2.1a). However, as external forces are not necessarily a constant, the curvatures of a G-FMPES are generally expected to be different from those of the unmodified PES. The effect of varying curvatures is discussed in Sect. 2.2.4.

2.2.3 Pseudo-Hydrostatic Pressure

As an example of a non-constant external force, we use a force vector referred to as "pseudo-hydrostatic pressure," where, the external force applied *on each atom*, $\mathbf{f}_{\text{ext}}^{(j)}$, is calculated as

$$\mathbf{f}_{\text{ext}}^{(j)} = P_{HP}\left[\mathbf{r}^{(j)} - \mathbf{c}\right]; \quad \forall \quad j = 1, 2, 3 \ldots N \tag{2.11}$$

where P_{HP} is a user-defined constant with units of kcal mol^{-1} Å^{-2}, $\mathbf{r}^{(j)}$ is the position vector of the jth atom, and $\mathbf{c}$ is the geometric centroid. Here, lowercase boldface symbols refer to 3-dimensional vectors. A negative value of P_{HP} implies compression, while a positive value implies expansion. Also, both the magnitude and the direction of the external force on each atom are a function of the configuration. Consequently, the external force vector on all atoms, $\mathbf{F}_{\text{ext}}$ is a function of the current configuration and is different, and not constant. This scheme for the application of external forces is equivalent to placing each atom of the system in the same parabolic potential centered at the geometric centroid $\mathbf{c}$. It results in a conservative force field, thereby satisfying the assumptions made in deriving Eq. (2.6). For the interested reader, a proof that the force field is conservative is available in Appendix 1.

2.2.4 Transition Rates on the G-FMPES

There are two key differences in calculating transition rates on a G-FMPES when compared with on an unmodified PES, and can be understood within the context of harmonic Transition State Theory (h-TST), where transition rates are computed as

$$\overline{k} = \overline{k}_0 \exp\left[-\frac{\overline{E}_a}{k_B T}\right] \tag{2.12}$$

where k_B is the Boltzmann constant, T is the temperature, $\overline{E}_a$ is the activation energy for a transition, and $\overline{k}_0$ is the prefactor (related to the curvature).

The activation energy, $\overline{E}_a$, is simply the difference in energies of the saddle point and the energy minimum on the G-FMPES. From Eq. (2.6), it is easy to see that stationary points on a G-FMPES (i.e., points with $\nabla\overline{V}(\mathbf{R}) = 0$) are in general different from those on an unmodified PES, and consequently, the activation energy for a transition can be expected to be different on a G-FMPES. Calculating the activation energy requires finding the saddle point configuration, which can be achieved using any of the various saddle point finding methods [46], and indeed, many researchers have accounted for this change [4, 29, 30] in the activation energy of a transition when computing transition rates.

However, these very studies have neglected the effects of curvature changes, which affect transition rates via the prefactor $\overline{k}_0$ with the justification that most significant changes in transition rates are due to changes in the activation energy, and therefore overwhelms any effects from curvature changes that manifest themselves in the prefactor. While this assumption may be acceptable in many situations, transitions with unusual prefactors such as the transformation of voids to stacking fault tetrahedra [47] with a prefactor tens of orders of magnitude higher than typical exist, and can be expected to show counterintuitive changes in transition rates when the external force is not a constant.

The effects of curvature change can be understood in the context of Vineyard's expression [48]:

$$\overline{k}_0 = \frac{\prod_{j=1}^{3N-m} \overline{\nu}_j^{(\min)}}{\prod_{j=1}^{3N-(m+1)} \overline{\nu}_j^{(\text{sad})}} \tag{2.13}$$

where the $3N - m$ different $\overline{\nu}_j^{(\min)}$ are the non-zero normal mode frequencies of the energy minimum, and the $3N - (m + 1)$ different $\overline{\nu}_j^{(\text{sad})}$ are the positive, non-zero normal mode frequencies of the saddle point. Subtraction of m in the numerator accounts for the m rigid body motion degrees of freedom, and subtraction of $(m + 1)$ in the denominator accounts for the rigid body motion degrees of freedom plus 1 imaginary frequency for a first-order saddle point. For systems with translational and rotational symmetry, $m = 6$. Application of external forces can break the symmetry, resulting in $m \leq 6$. These normal mode frequencies are in turn calculated by diagonalizing the Hessian matrix $\overline{\mathbf{H}}(\mathbf{R}) = \mathbf{H}(\mathbf{R}) + \mathbf{H}_{\text{ext}}(\mathbf{R})$.

For a constant external force resulting in $\mathbf{H}_{\text{ext}}(\mathbf{R}) = 0$, the prefactor $\overline{k}_0$ is calculated using the curvature of the unmodified PES at the locations of the new stationary points.

2.3 Applications

With the above understanding of how to compute energies, forces, and curvatures on a G-FMPES, standard atomistic techniques were used to compute quantities of practical interest. In this chapter, we will outline the effects of pseudo-hydrostatic pressure on reaction rates for (i) conformation transitions in ethane and RDX [1], (ii) the decomposition of RDX [3], and (iii) a Diels-Alder reaction [2].

Energies and their gradients (forces) on the unmodified PES (namely $V(\mathbf{R})$ and $\nabla V(\mathbf{R})$) were evaluated using an *Ab initio* electronic structure method with suitable basis sets, as implemented in the AIMS-MOLPRO code [49]. This combination of method and basis is a computationally inexpensive means of illustrating the main point of this chapter: the calculation of static quantities on a G-FMPES and their comparison with corresponding quantities on an unmodified PES. Transition states were calculated using the Nudged Elastic Band (NEB) method with the improved tangent estimate [50–52]. A more detailed description of our implementation is available in Appendix 2. Structure optimizations were performed using the Fast Inertial Relaxation Engine (FIRE) [53]. The integral in Eq. (2.6) was computed using the trapezoidal rule over a grid with resolution 5×10^{-3} Å along a straight line between $\mathbf{R}$ and $\mathbf{R}_{\text{ref}}$. Hessians of all stationary points on the G-FMPES had 6 numerically zero eigenvalues corresponding to translation and rigid body rotation. Hessians of all saddle points had only one negative eigenvalue, thereby ensuring that they were true first-order saddle points.

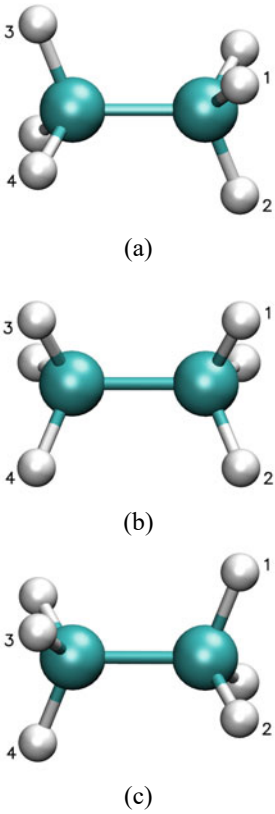

Fig. 2.2 Rotation of a CH_3 group by 120° about the C–C bond in ethane. **a** Start state—often referred to as the staggered conformation **b** Saddle point or eclipsed conformation (c) End state—also a staggered conformation. Reprinted (adapted) from [1], with the permission of AIP publishing

2.3.1 Rotational Barrier in Ethane

Using the Hartree-Fock (HF) method [54–56] with the 6-31G** basis set [57], we first examined the rotational energy barrier in ethane (C_2H_6): a 120° rotation of a CH_3 group about the C–C bond of an ethane molecule, as shown in Fig. 2.2. This transition is a prototypical example for understanding steric hindrance, first discovered by Kemp and Pitzer [58] who showed that a rotational barrier of 2.8 kcal mol^{-1} had to be present in order to obtain thermodynamic quantities in agreement with the experiment.

For this transition, the reference configuration was chosen to be the staggered conformation at $P_{HP} = 0$. Figure 2.3a shows the energy along the reaction coordinate for this transition at various pressures, and all energies are relative to the reference configuration. The nominal energy (no external pressure) was 3.02 kcal mol^{-1}, within 8% of the experimental value of 2.8 kcal mol^{-1} [58, 59]. With increasing compression (or decreasing values of P_{HP}), the saddle point energy of the saddle point progressively increases, while the energy of the staggered conformation decreases, thereby

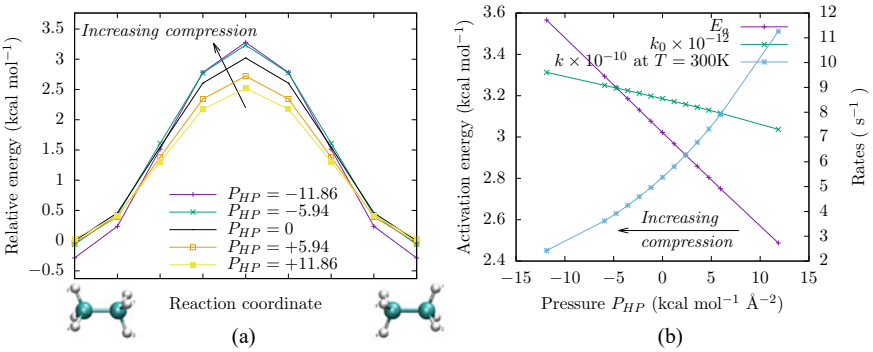

Fig. 2.3 For the rotational transition of ethane, **a** energy along the reaction coordinate as a function of pressure for the values of P_{HP} (in kcal mol^{-1} Å^{-2}) indicated in the legend, and **b** activation energies, prefactors, and transition rates as a function of pressure. All energies are relative to that of the staggered configuration at zero pressure. In both figures, an arrow indicates the direction of increasing compression. Reprinted (adapted) from [1], with the permission of AIP publishing

leading to a net increase in activation energy as a function of increasing compression. There is a corresponding increase in the prefactor with increasing compression (see Fig. 2.3), but this increase is overshadowed by the increase in activation energy, and consequently, there is a net decrease in the transition rate as a function of increasing compression.

Wavenumbers of the staggered conformation of ethane computed by diagonalizing the Hessian are given in Table 2.1 in units of inverse centimeters. The wavenumbers at zero pressure are in good agreement with the values available in the literature for calculations at the HF/6-31G** level of theory [60]. Compression shifts the spectrum to higher wavenumbers (blueshift) indicating that the modes become stiffer, while expansive pressures have the opposite effect, i.e., redshift the spectrum. This behavior is qualitatively consistent with the experimental behavior seen by Kurnosov et al. [61] who saw that the Raman spectra of both liquid and solid ethane shifted to higher wavenumbers with increasingly compressive pressure over a range of up to 6900 MPa.

2.3.2 *Conformational Transformations in RDX*

The second molecule examined was RDX, also known as hexahydro-1,3,5-trinitro-*s*-triazine, and is an energetic molecular crystal and is used in many explosive formulations. RDX has a chemical formula $C_3H_6N_6O_6$, and is shown in Fig. 2.4. Red atoms are oxygen and are part of the nitro (NO_2) groups, blue atoms are nitrogen, and cyan atoms are carbon. The ring formed by alternating C and N atoms is the triazine ring, and the nitro groups are on the side. The position of the nitro side groups with respect to the triazine ring as determined by the angle between the N−N bond and

Table 2.1 Calculated wavenumbers (in cm^{-1}) of the staggered conformation of ethane for the lowest, zero, and highest values of pseudo-hydrostatic pressure, P_{HP} (in kcal $mol^{-1}Å^{-2}$), studied

$P_{HP} = -11.86$	$P_{HP} = 0$	$P_{HP} = 11.86$
382.80	327.65	264.69
897.95	885.11	846.16
897.95	885.16	876.95
1208.96	1059.31	876.96
1366.90	1329.27	1281.82
1366.91	1329.31	1281.82
1510.56	1531.93	1538.96
1574.90	1564.79	1546.27
1648.04	1627.73	1601.37
1648.12	1627.81	1601.43
1651.56	1632.78	1612.73
1651.64	1632.86	1612.79
3344.70	3180.24	2992.31
3351.69	3185.88	2995.89
3423.52	3234.15	3020.84
3423.60	3234.22	3020.91
3445.54	3259.17	3047.84
3445.61	3259.23	3047.90

The wavenumbers of the rigid body modes of deformation are not reported
Adapted from [1]

the plane of the C−N−C triple (axial, intermediate, or equatorial, denoted by a, i, or e, respectively). Molecular dynamics simulations using a non-reactive and fully-flexible force fields have shown that conformational transitions play an important role in the stability of high-pressure phases [34], plastic deformation mechanisms of RDX [38, 62–64], and contribute to energy concentration in strained α-RDX crystals [33].

We studied the Caaa ↔ Ceee transition (shown in Fig. 2.4) of an isolated RDX molecule because it has the highest activation energy of all the transitions between conformers for an RDX molecule with the Chair shaped triazine ring. The pseudo-hydrostatic pressures applied in this test case are particularly relevant because the deviatoric part of the stress tensor vanishes for the gas phase and the pressure $(-\mathrm{tr}(\boldsymbol{\sigma})/3)$ becomes the critical term at high stresses and temperatures under which decomposition of shocked explosives takes place.

For this transition, the Caaa conformer at $P_{HP} = 0$ was chosen as the reference configuration $\mathbf{R}_{\mathrm{ref}}$ with $V_{\mathrm{ext}}(\mathbf{R}_{\mathrm{ref}}) = 0$. Increasingly compressive pressures increased the energy barrier for the forward (Caaa → Ceee) transition while decreasing the barrier for the reverse (Caaa ← Ceee) transition with a concomitant increase (or decrease) in the net rates (see Fig. 2.5). For high compressions, with pseudo-hydrostatic pressures with $P_{HP} \leq -2.37$ kcal mol^{-1} $Å^{-2}$, the Ceee conformer was

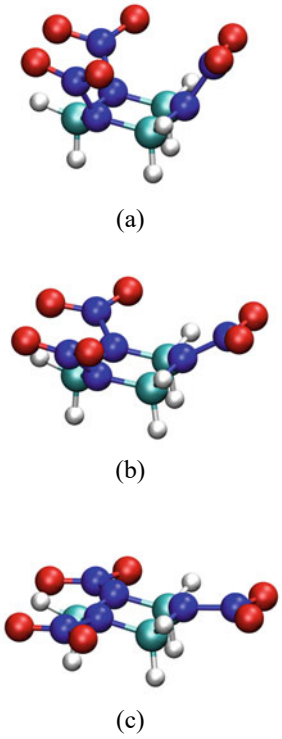

Fig. 2.4 Transition of an RDX molecule ($C_3H_6N_6O_6$) from the Caaa conformer to Ceee. **a** Caaa conformer, **b** saddle point, and **c** Ceee conformer. The red atoms are oxygen, and are part of the nitro (NO_2) groups, blue atoms are nitrogen, and cyan atoms are carbon. The ring formed by alternating C and N atoms is the triazine ring. Reprinted (adapted) from [1], with the permission of AIP publishing

no longer stable, and spontaneously transitioned into the Caaa conformer. Conversely, for low compressions with pseudo-hydrostatic pressures with $P_{HP} \geq 1.78$ kcal mol^{-1} Å^{-2}, the Caaa conformer was no longer stable and spontaneously transformed into the Ceee conformer.

This mechanism where external stresses lead to the disappearance of stationary points on the energy landscape has been observed before in the case of zirconium interstitials [29], and indicates that an energy minimum merges with a saddle point. It is entirely possible that new stationary points may be introduced by external stresses.

As with the case of ethane, we see that higher compressions cause the RDX molecule to adopt more compact conformations leading to enhanced steric effects. This observation agrees well with the fact that Caaa is present in the high-pressure polymorphs (β and ε) of RDX [67, 68]. For the Caaa $\rightarrow$ Ceee transition, we see that the transition rate decreases with increasing compression. However, the backward transition (Caaa $\leftarrow$ Ceee) rate increases with increasing compression, and this is

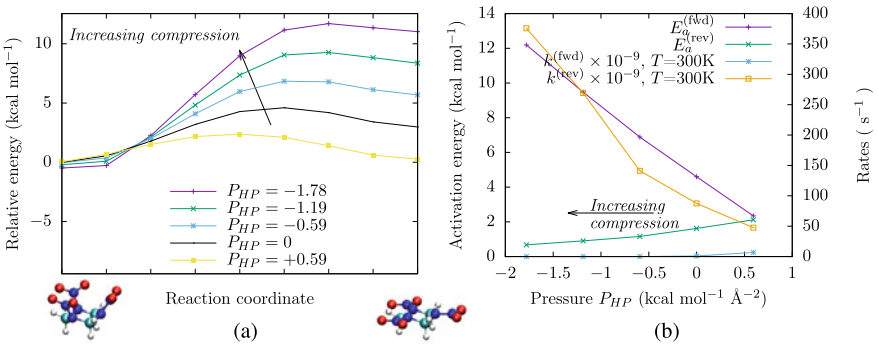

Fig. 2.5 For the Caaa to Ceee transition of RDX, **a** energy along the reaction coordinate as a function of pressure for the values of P_{HP} (in kcal mol^{-1} Å^{-2}) indicated in the legend, and **b** activation energies, prefactors, and transition rates as a function of pressure. Here, the forward transition is the Caaa → Ceee transition. All energies are relative to that of the Caaa conformation at zero pressure. In both figures, an arrow indicates the direction of increasing compression. Reprinted (adapted) from [1], with the permission of AIP publishing

thought to be because the Ceee conformer is a higher-energy conformer where steric effects are already pronounced (as evidenced by it being unstable at high compressions) and the extra compression serves to make transitions out of this high-energy conformer more accessible.

Table 2.2 shows the calculated wavenumbers with units of cm^{-1} of the two conformations for the lowest, zero, and highest values of pseudo-hydrostatic pressure used in this study. Again, as with the case of ethane, the harmonic vibrational spectrum of RDX shifts to higher wavenumbers with increasing compression. This is consistent with independent experimental studies [69–71], as well as molecular dynamics studies [72]. The softer modes of Ceee, from 54 to 122 cm^{-1}, however, behave in the opposite manner. Also shown in Table 2.2 are the wavenumbers obtained from DFT studies by Rice and Chabalowski [65] (at the B3LYP/6-31G** level), as well as experimental data from the vapor phase [66]. While there is general agreement between our harmonic frequencies and those of the experiment, there are significant differences between our frequencies and those of Rice and Chabalowski [65], but we suspect this is due to the differences in electronic structure theory techniques employed.

2.3.3 *Decomposition Mechanism of RDX*

We studied the three decomposition mechanisms of RDX shown in Fig. 2.6. In our study, all calculations were carried out with RDX in a chair conformation with all NO_2 groups in the axial position (Caaa), claimed to be the global minimum [65, 73–75] studies. All stationary points were characterized by performing frequency

Table 2.2 Calculated wavenumbers (in cm^{-1}) of the two conformers of RDX for the lowest, zero, and highest values of pseudo-hydrostatic pressure, P_{HP} (in kcal $mol^{-1}Å^{-2}$), studied

DFT, Ref. [65]	Experimental Ref. [66]	This work, Caaa			This work, Ceee		
		$P_{HP} = -1.78$	$P_{HP} = 0$	$P_{HP} = 0.59$	$P_{HP} = -1.78$	$P_{HP} = 0$	$P_{HP} = 0.59$
31		43.16	35.64	17.97	54.07	54.67	57.61
37		46.87	35.85	18.98	54.24	54.91	57.72
63		46.92	66.61	52.48	58.41	69.43	74.24
67		124.51	77.24	80.61	83.42	89.03	90.61
100		147.74	109.04	100.29	117.10	122.78	125.56
102		148.16	109.20	100.41	117.17	122.88	125.60
220		252.57	242.29	226.39	190.72	187.66	188.00
221		252.89	243.26	227.50	190.85	187.96	188.13
301		328.25	342.44	353.29	258.64	242.31	237.75
363		433.26	408.85	392.75	258.82	242.62	237.89
365		433.84	409.58	393.09	354.65	323.37	312.62
409		490.40	465.49	442.88	392.41	378.23	373.04
413		490.50	465.54	442.96	413.76	402.22	398.37
442		542.98	508.24	480.28	413.81	402.58	398.50
458		581.23	534.35	500.34	413.87	402.70	398.55
590		665.53	665.83	666.88	662.87	653.23	649.50
590		678.61	669.92	667.07	662.91	653.35	649.54
593		678.62	670.09	670.71	763.07	748.61	744.02
660		743.83	736.41	736.48	804.80	791.93	787.26
661	782	744.39	737.15	736.95	804.85	791.98	787.28
749	845	838.31	847.56	854.82	888.82	888.90	888.52
753	880	893.85	889.89	887.55	905.48	900.70	899.43
754		894.12	890.18	887.70	905.54	900.76	899.45
782	910	927.25	911.05	900.68	926.74	919.71	917.42
863		977.35	965.23	961.49	1025.01	1000.65	993.22
864		977.39	965.30	961.58	1025.04	1000.66	993.23
887		994.59	972.64	964.37	1039.98	1007.40	997.06
906	1014	1054.98	1048.14	1049.12	1132.72	1121.19	1118.04
907		1055.04	1048.31	1049.38	1132.73	1121.31	1118.09
935		1103.13	1096.06	1096.06	1158.32	1137.97	1131.37
1005		1183.59	1177.26	1181.35	1245.16	1222.61	1214.21
1005	1218	1183.95	1177.81	1181.77	1245.22	1222.61	1214.22
1141	1268	1299.40	1289.72	1291.61	1335.81	1319.68	1313.45
1242	1319	1414.78	1400.56	1399.42	1425.35	1403.41	1393.44
1250	1374	1415.18	1401.04	1399.72	1438.70	1407.28	1397.35
1252		1421.61	1414.65	1403.04	1464.11	1439.33	1430.03
1275	1420	1436.76	1418.06	1421.94	1464.18	1439.46	1430.07
1292	1444	1494.98	1494.98	1497.76	1476.04	1458.18	1451.63
1294		1520.75	1511.62	1505.00	1476.08	1458.33	1451.70
1345		1520.77	1511.83	1505.27	1525.41	1518.57	1516.90
1363		1541.13	1531.23	1528.75	1558.34	1537.31	1530.36

(continued)

Table 2.2 (continued)

DFT, Ref. [65]	Experimental Ref. [66]	This work, Caaa			This work, Ceee		
		$P_{HP} = -1.78$	$P_{HP} = 0$	$P_{HP} = 0.59$	$P_{HP} = -1.78$	$P_{HP} = 0$	$P_{HP} = 0.59$
1381		1541.77	1531.81	1528.99	1558.37	1537.38	1530.43
1384	1584	1585.01	1578.37	1577.65	1636.15	1612.26	1603.91
1402		1585.06	1578.44	1577.72	1636.37	1623.96	1619.76
1403		1598.31	1589.11	1585.93	1636.42	1624.01	1619.80
1464		1619.50	1616.34	1618.19	1657.76	1654.11	1653.79
1466		1619.53	1616.43	1618.31	1657.80	1654.11	1653.79
1482		1665.26	1655.60	1653.42	1670.68	1668.21	1667.74
1627		1854.72	1845.01	1839.91	1864.45	1848.85	1843.95
1658		1914.64	1890.13	1877.62	1889.74	1873.60	1868.46
1658		1914.99	1890.69	1878.07	1889.96	1873.61	1868.48
3064	3065	3311.08	3266.08	3245.22	3188.21	3172.70	3167.49
3064		3311.42	3266.52	3245.39	3188.29	3172.81	3167.52
3070		3323.14	3276.76	3254.68	3196.56	3179.52	3173.78
3192		3476.09	3434.69	3419.39	3484.77	3431.28	3412.98
3192		3476.20	3434.73	3419.44	3484.82	3431.33	3413.01
3194		3477.51	3436.30	3421.24	3487.38	3433.89	3415.59

The wavenumbers of the rigid body modes of deformation are not reported. For comparison, wavenumbers obtained by Rice and Chabalowski [65] for the Caaa conformer using a B3LYP functional, as well as experimental data from the vapor phase obtained by Karpowicz and Brill [66] are shown

Adapted from [3]

calculations. The zero-point energy (ZPE) correction to the electronic energy was included for all stationary points, and the ZPE is included in all energy values.

2.3.3.1 Concerted Mechanism

In the concerted mechanism, all three C−N bonds of RDX are broken simultaneously, yielding three molecules of CH_2-N-NO_2 (methylenenitramine, MN). The transition state (TS) is shown in Fig. 2.7a). The breaking C−N distances are between 2.00 Åand 2.14 Å. external forces modify the PES, altering both E_a and E_{rxn}. Furthermore, the sign of the applied external forces modifies the PES in different ways. A positive value of P_{HP} decreases the height of the reaction barrier and makes the reaction more exothermic. For the two highest values of P_{HP} we considered, the concerted reaction becomes exothermic, while for all other values of P_{HP} the reaction is endothermic. At all P_{HP} values, the mechanism remains concerted except for the two highest compressive values. In these last two cases, one of the C−N bonds breaks first followed by the simultaneous fission of the other two C−N bonds—a fundamental change in the reaction pathway (Table 2.3).

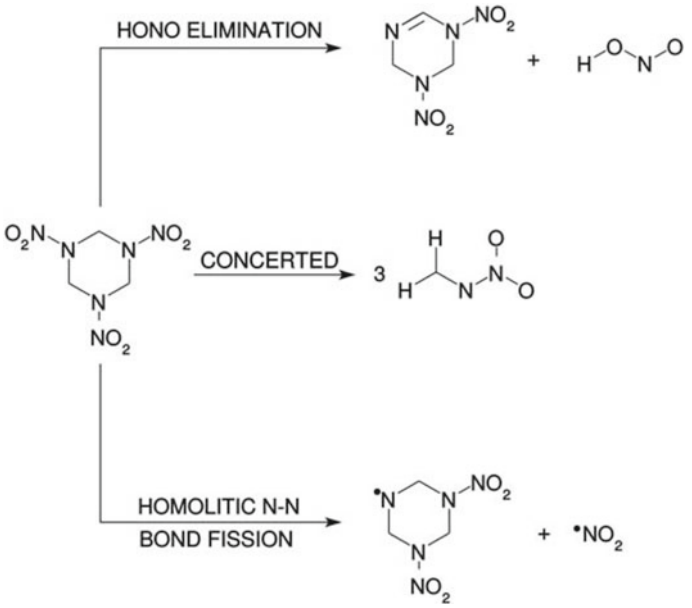

Fig. 2.6 Schematic of the initial decomposition reactions of RDX. Reprinted (adapted) from [3] with the permission of John Wiley & Sons

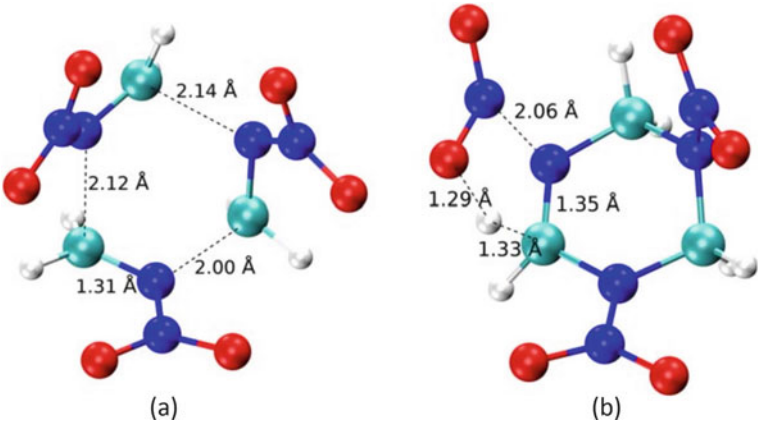

Fig. 2.7 Transition states of **a** concerted mechanism and **b** HONO elimination. Atom colors: C in cyan, N in blue, O in red, and H in white. Reprinted (adapted) from [3] with the permission of John Wiley & Sons

Table 2.3 Calculated activation (E_a) and reaction (E_{rxn}) energies at different values of pseudo-hydrostatic pressure, P_{HP} (in kcal mol^{-1} Å^{-2}), for concerted mechanism

P_{HP}	This work		Reference [73]	
	E_a	E_{rxn}	E_a	E_{rxn}
0	59.9	35.1	59.4	45.9
Expansion				
1.255	54.1	−16.9	.....	.....
0.941	57.2	−3.9	.....	.....
0.188	59.6	27.2	.....	.....
0.063	59.8	32.6	.....	.....
Compression				
−0.063	60.1	37.7	.....	.....
−0.188	60.6	42.8	.....	.....
−0.941	70.4	68.5	.....	.....
−1.255	77.1	76.0	.....	.....

All energies are expressed in kcal mol^{-1}
Adapted from [3]

2.3.3.2 HONO Elimination

In another possible decomposition mechanism of RDX, the close contact between one NO_2 group and one H leads to the elimination of one HONO molecule. The geometry of the TS found for this mechanism is shown in Fig. 2.7b. The calculated E_a for this mechanism is equal to 37.9 kcal mol^{-1}, while the E_{rxn} is equal to −10.1 kcal mol^{-1}. Both E_a and E_{rxn} make the HONO elimination a more favorable decomposition pathway than the concerted mechanism: the energy barrier for HONO elimination is ∼20 kcal mol^{-1} lower than that of the concerted mechanism, and moreover, the HONO elimination is exothermic. The effect of external forces on this mechanism was minor (less than 1 kcal mol^{-1}), so we do not discuss this further (Table 2.4).

2.3.3.3 Homolytic N−N Bond Fission

A third decomposition mechanism of RDX starts via the homolytic fission of one of the N−N bonds. The N−N fission proceeds through a loose TS, associated with a large pre-exponential factor in the correlated rate constant [73, 76, 77]. We found a dissociation energy of 36.1 kcal mol^{-1} for this reaction. This value is in good agreement with previously calculated dissociation energies of RDX [73, 74, 78] ranging between 34 kcal mol^{-1} and 42 kcal mol^{-1}. The dissociation energy barrier for the N−N fission (36.1 kcal mol^{-1}) is very close to the energy barrier of the HONO elimination (37.9 kcal mol^{-1}). HONO elimination and N−N fission are very likely the favored starting routes for the decomposition of RDX. In a recent study using coupled-cluster theory, Molt et al. found a "true" TS for the N−N fission [79]. Molt et

Table 2.4 Calculated activation (E_a) and reaction (E_{rxn}) energies at different values of pseudo-hydrostatic pressure, P_{HP} (in kcal mol^{-1} Å^{-2}), for HONO elimination mechanism

P_{HP}	This work		Reference [73]	
	E_a	E_{rxn}	E_a	E_{rxn}
0	37.9	−10.1	39.2	−8.5
Expansion				
0.314	37.3	−28.7	.....	.....
0.188	37.5	−21.3	.....	.....
0.126	37.7	−17.8	.....	.....
0.063	37.7	−13.9	.....	.....
Compression				
−0.063	38.0	−6.4	.....	.....
−0.126	38.0	−3.2	.....	.....
−0.188	38.1	0.8	.....	.....
−0.314	38.4	7.9	.....	.....

All energies are expressed in kcal mol^{-1}
Adapted from [3]

al. calculated an energy barrier more than 10 kcal mol^{-1} higher than our and previous estimates [73, 74, 78], concluding that the N−N fission perhaps does not compete with the HONO elimination. The effect of external forces on the N−N fission (see Table 2.5) shows the same trend as for the two other mechanisms. The application of a compressive force works in opposition to the decomposition reaction, increasing the dissociation barrier, while the application of an expansive force lowers the barrier. Moreover, at the two highest positive values of P_{HP} that we considered, the N−N fission becomes exothermic.

2.3.4 A Diels-Alder Reaction

The Diels-Alder (DA) reaction, where a diene reacts with a dienophile to form a cyclohexene derivative is an important route for synthesizing numerous cyclic compounds, and has been widely studied [80–95]. The simplest DA reaction, often called the parent DA reaction, is a [4 + 2] cycloaddition between 1,3-butadiene and ethylene which results in the formation of cyclohexene. DA reactions are used to synthesize a wide variety of compounds, such as pharmaceuticals [96–99], agrochemicals, as well as flavors, and fragrances [100].

In this section, we examine the effects of compressive external forces designed to mimic hydrostatic pressures on the mechanism of parent DA reaction between butadiene and ethylene using. As with other reactions outlined in this chapter, MEPs and transition states on the G-FMPES were calculated using a climbing-image nudged elastic band (CI-NEB) method [50, 51]. The levels of theory employed, how-

Table 2.5 Calculated reaction energies (E_{rxn}) at different values of pseudo-hydrostatic pressure, P_{HP} (in kcal mol^{-1} Å^{-2}), for homolytic N–N bond fission

P_{HP}	This work E_{rxn}	Reference [73] E_{rxn}
0	36.1	39.0
Expansion		
0.628	−58.6	.....
0.314	−6.3	.....
0.188	4.7	.....
0.063	25.6	.....
Compression		
−0.063	46.5	.....
−0.188	67.5	.....
−0.314	88.5	.....
−0.628	135.6	.....

All energies are expressed in kcal mol^{-1}
Adapted from [3]

ever, were CASSCF(6,6)/6-31G** [57, 101, 102], and B3LYP-DFT/6-311++G**, because while CASSCF is appropriate for studying organic chemical reactions [6, 103, 104], it often underestimates reaction exothermicity [105, 106], and energies calculated using the DFT method are known to provide a better match with experimental data. In this chapter, some experimentally testable predictions about the exothermicity, reaction rates, and the ratio of yield of the main reaction to the yield of the undesirable side reaction are made.

Experimentally, the activation energy of the parent DA reaction has been measured as 27.5 ± 2 kcal mol^{-1} [105, 107], and amongst much discussion, [103, 105, 108–121], is thought to have two mechanisms: a single-step concerted mechanism, and a two-step diradical mechanism. An undesirable side reaction is the formation of vinylcyclobutane [122]. These different pathways are depicted in Fig. 2.8. The concerted mechanism (Fig. 2.8, a → c) is a single-step process and results in the simultaneous formation of two new σ-bonds between the carbon atoms of butadiene and ethylene. The two-step mechanism (Fig. 2.8, a → b → c) involves a first transition to a stable diradical intermediate, followed by a second transition into cyclohexene. The third pathway (Fig. 2.8, a → d) is the undesirable side reaction that forms vinylcyclobutane.

2.3.4.1 Concerted Mechanism

In Fig. 2.9, we see the optimized geometries and bond lengths (in Å) of the reactants, transition state, and product on the unmodified PES. As the reaction progresses, the terminal methylene groups of the reactants rotate such that the protons (H) are

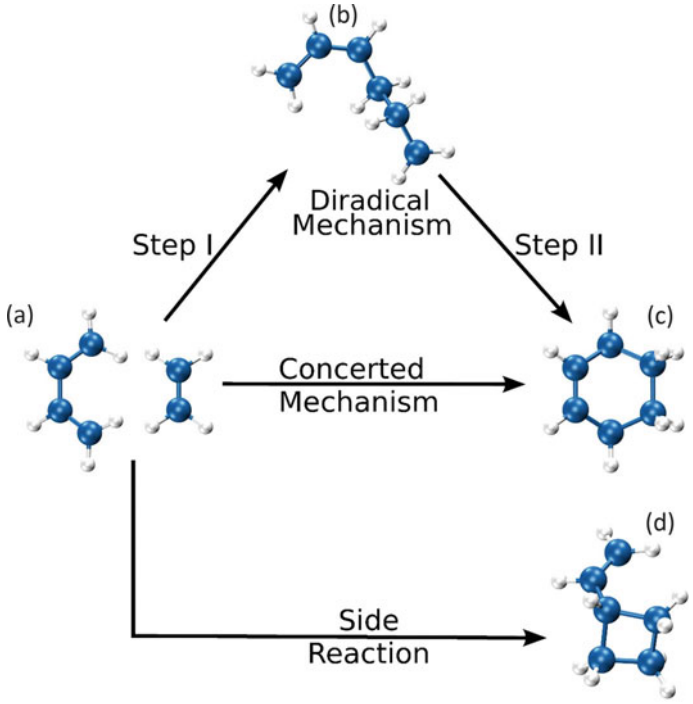

Fig. 2.8 Schematic of the parent DA reaction and the undesirable side reaction with structures of **a** butadiene and ethylene, **b** diradical, **c** cyclohexene, and **d** vinylcyclobutane. Atom colors: C in cyan, and H in white. Reprinted (adapted) from [2], with the permission of AIP publishing

repelled outwards. Geometries of the reactants, transition state, and product suggest that bond formation between C1−C5 and C4−C6 occurs to the same extent. The length of the C2−C3 bond shrinks from 1.48 Å to 1.36 Å, indicating a single → double bond transition, while that of the C5−C6 bond increases from 1.34 Å to 1.58 Å, indicating a double → single bond transition.

In Fig. 2.10, we see energies along the reaction pathway obtained using CASSCF (Fig. 2.10a) and DFT (Fig. 2.10b) methods. The energies of the reactants (butadiene + ethylene) have been shifted to zero. In the absence of any external pressure, the pathway obtained is shown by the black curve (with a filled circle) for both methods. Table 2.6 summarizes activation energies and reaction energies obtained in our calculations, and a comparison with values obtained by other simulations [105, 119] and experiments [107, 123]. We find that this reaction is exothermic with a reaction energy of −21.2 kcal mol^{-1}, and an energy barrier of 45.5 kcal mol^{-1}, and these values are comparable with other simulation results [119, 121]. Experimentally determined values [107, 123] are, however, significantly different and we believe that this discrepancy is because the CASSCF method is known to underestimate reaction exothermicity [105, 119, 121]. The B3LYP-DFT method, on the other hand, with a

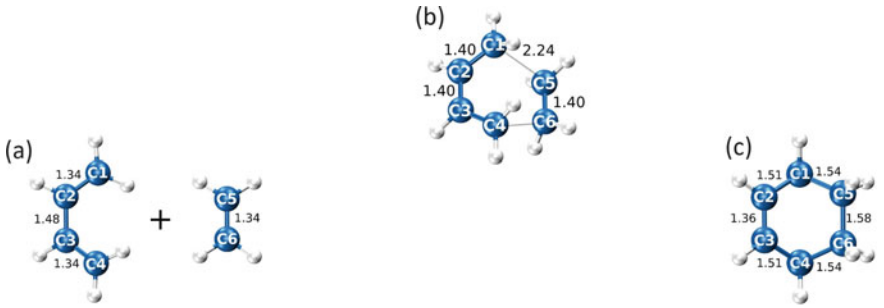

Fig. 2.9 Optimized structures of **a** reactants (butadiene and ethylene), **b** transition state, and **c** product (cyclohexene) of the parent DA reaction in the absence of external pressure, i.e., $P_{HP} = 0$. The shrinkage of the C2–C3 bond from 1.48 Å to 1.36 Å is consistent with the formation of a double bond. Reprinted (adapted) from [2], with the permission of AIP publishing

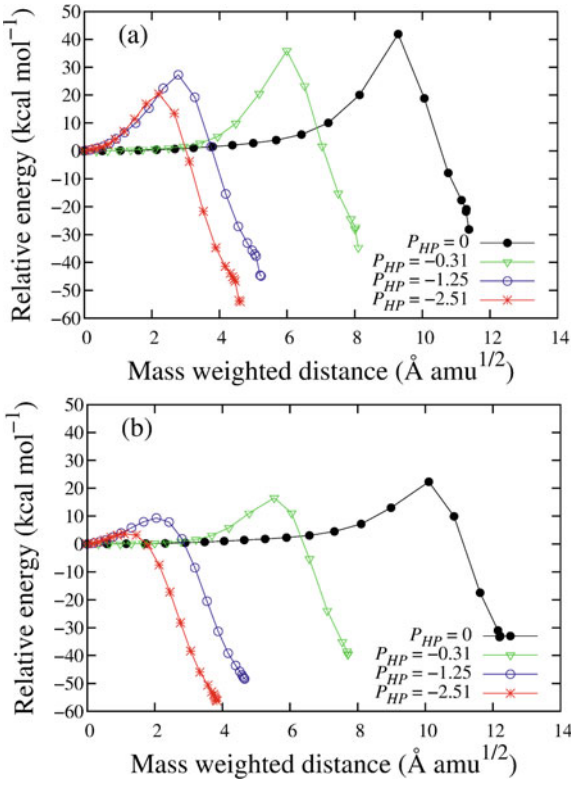

Fig. 2.10 Energy along the reaction coordinate as a function of pseudo-hydrostatic pressure, P_{HP}, for the concerted mechanism calculated at **a** CASSCF(6,6) and **b** B3LYP-density functional theory levels. The values of P_{HP} (in kcal mol^{-1} Å^{-2}) used in our simulation are indicated in the legend. Lower values of P_{HP} correspond to increasing compression due to the definition in Eq. (2.11). The energies of the reactants (butadiene + ethylene) are shifted to zero in all cases. The increasing compression lowers the energy barrier, and makes the reaction more exothermic. The vibrational ZPE correction has not been included in these plots. Reprinted (adapted) from [2], with the permission of AIP publishing

Table 2.6 Comparison of activation (E_a) and reaction (E_{rxn}) energies obtained in our calculations, calculations by other groups, as well as experimental values for the concerted mechanism

Energies	Previous studies			This work	
	Experimental	CASSCF(6,6)/ 6-31G** [119]	B3LYP/ 6-31G* [105]	CASSCF(6,6)/ 6-31G**	B3LYP/ 6-311++G**
E_a	27.5 ± 2 [107]	44.5	24.8	45.5	24.3
E_{rxn}	−40.0 [123]	−14.9	−36.6	−21.2	−27.6

All energies are expressed in kcal mol^{-1}
Adapted from [2]

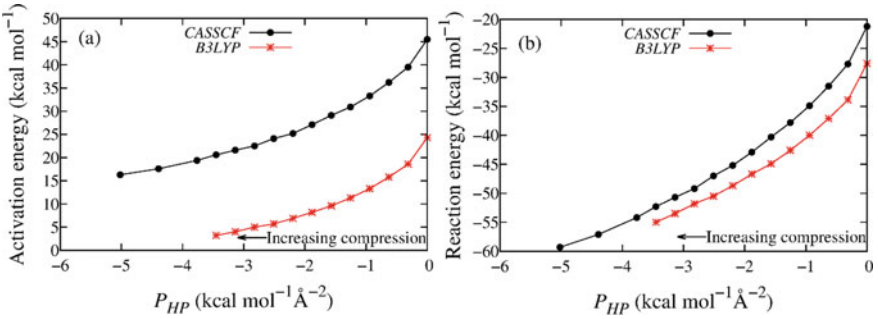

Fig. 2.11 **a** Activation energy, and **b** reaction energy as a function of compressive pseudo-hydrostatic pressure, P_{HP}, for the concerted mechanism between butadiene and ethylene. The dependence of both these quantities is a non-linear function of P_{HP}, implying that Bell's theory might not be valid for this system. Reprinted (adapted) from [2], with the permission of AIP publishing

higher basis set and diffuse functions (6-311++G**) results in computed activation energy of 24.3 kcal mol^{-1}, comparable with the experimental value of 27.5 ± 2 kcal mol^{-1} [107].

Effects of compressive pseudo-hydrostatic pressure on the systems are also shown in Fig. 2.10, with energies of the reactants (butadiene + ethylene) shifted to zero. As the magnitude of compression increases, the transition state shifts toward the reactants. Compression also lowered the activation energy for the concerted pathway, with higher compression resulting in lower activation energies. At the B3LYP level, reactants transitioned spontaneously to cyclohexene for $P_{HP} < -3.45$ kcal mol^{-1} Å^{-2}.

In Fig. 2.11a, we show the dependence of activation energy on compressive pseudo-hydrostatic pressure, P_{HP}. The relationship appears to be non-linear, and in violation of Bell's theory [124]. In Fig. 2.11b, we show shows the reaction energy as a function of P_{HP}, and it appears that reaction exothermicity increases with compression, and this dependence is also non-linear. These data indicate that the parent DA reaction becomes more exothermic with increasing compressive pseudo-hydrostatic pressure—an experimentally testable prediction.

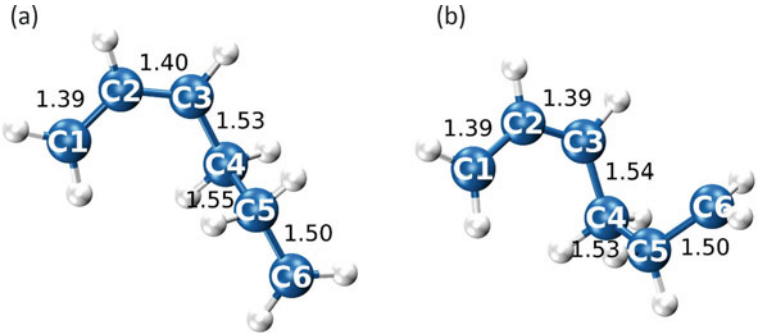

Fig. 2.12 Geometries of the **a** anti, and **b** gauche-diradical intermediates for the two-step diradical mechanism. C–C bond lengths are in Å. Reprinted (adapted) from [2], with the permission of AIP publishing

2.3.4.2 Two-Step Diradical Mechanism

This possible route for cyclohexene formation is depicted in Fig. 2.8, a → b → c. Here, C–C bonds are formed sequentially. The two-step reaction proceeds via a high-energy intermediate, called a diradical, of which there are two types. These types are referred to as the anti and gauche diradicals [105], as shown in Fig. 2.12. Unfortunately, the combination of DFT and NEB methods did not allow us to correctly describe the pathway on the PES for a system that switches spin state (singlet ↔ triplet) during the transition, viz., butadiene + ethylene → diradical → cyclohexene. Therefore, the diradical pathway was investigated only at the CASSCF level of theory.

We first discuss the anti-diradical pathway (Fig. 2.12a). Here, the reactants first form the anti-diradical, which then transitions into cyclohexene via torsional rotation about the C3−C4 and C4−C5 bonds. The energies along the reaction coordinate (expressed in the mass-weighted distance) as a function of P_{HP} are shown in Fig. 2.13. At $P_{HP} = 0$, the barrier for the formation of the anti-diradical is 44.0 kcal mol^{-1}, while the transition of the anti-diradical into cyclohexene was over a barrier of 3.9 kcal mol^{-1}. With increasing compression, the energy barrier for the formation of the anti-diradical decreased – this is likely because this process involves the translation of the molecules to form one bond, and the increasing compression facilitates this mechanism. The anti-diradical → cyclohexene transition involves rotation around C3−C4 and C4−C5 bonds, and we see that the energy barrier for this step increases with increasing compression. Here, increased compression results in the diradical becoming more compact, resulting in pronounced steric effects that increase the energy barrier. Beyond a critical value of compression ($P_{HP} \leq -2.51$ kcal mol^{-1}Å^{-2}), the anti-diradical becomes unstable, and is spontaneously converted into cyclohexene. The activation energies for the diradical mechanism as a function of pseudo-hydrostatic pressures, P_{HP}, are summarized in Table 2.7.

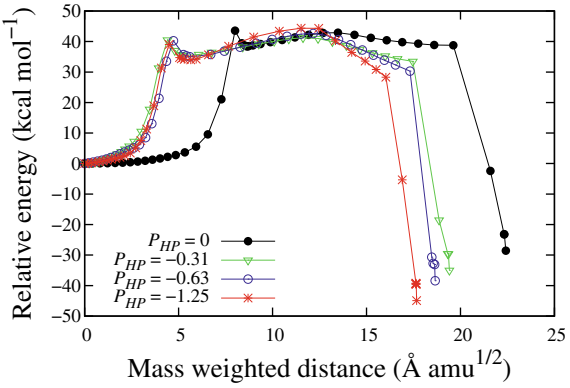

Fig. 2.13 Energy along the reaction coordinate as a function of pseudo-hydrostatic pressure, P_{HP}, for the two-step mechanism of DA reaction via the anti-diradical. The values of P_{HP} (in kcal mol^{-1} Å^{-2}) used in our simulation are indicated in the legend. The energies of the reactants (butadiene + ethylene) are shifted to zero in all cases. Increasing compression lowers the energy barrier for the first step, but raises the barrier for the second step. The vibrational ZPE correction has not been included in this plot. Reprinted (adapted) from [2], with the permission of AIP publishing

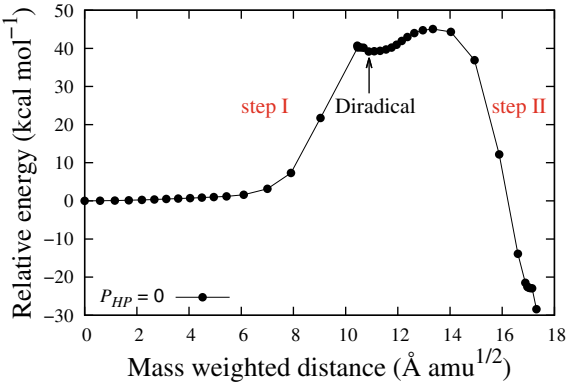

Fig. 2.14 Energy along the reaction coordinate for the two-step mechanism of DA reaction via the gauche-diradical. This reaction pathway was destabilized by the smallest value of compression that we attempted, viz., $P_{HP} = -0.31$ kcal mol^{-1}Å^{-2}, and the diradical spontaneously transitioned into vinylcyclobutane. The vibrational ZPE correction has not been included in this plot. Reprinted (adapted) from [2], with the permission of AIP publishing

Next, we discuss the gauche-diradical (Fig. 2.12b) pathway, whose MEP is shown in Fig. 2.14. Without compression, the barrier height for diradical formation (step I) is 41.4 kcal mol^{-1}, while the barrier for the diradical to transition into cyclohexene (step II) is 5.8 kcal mol^{-1}. The gauche-diradical is 0.9 kcal mol^{-1} below the transition state of step I. The activation energy of the overall reaction, defined as the highest peak along the MEP, is 46.3 kcal mol^{-1}. This activation energy is ∼1 kcal mol^{-1} more than that of the concerted pathway, and ∼2 kcal mol^{-1} more than that of the reaction

Table 2.7 Activation energies for diradical mechanism of DA reaction as a function of pseudo-hydrostatic pressure, P_{HP} (in kcal mol^{-1} Å^{-2}), calculated using CASSCF(6,6) level of theory

P_{HP}	Activation energy, E_a	
	Anti-diradical	Gauche-diradical
0	44.0	46.3
−0.31	43.6	.....
−0.63	43.0	.....
−1.25	44.3	.....

All energies are expressed in kcal mol^{-1}. For a non-zero value of P_{HP}, gauche-diradical is no longer a minimum in the PES
Adapted from [2]

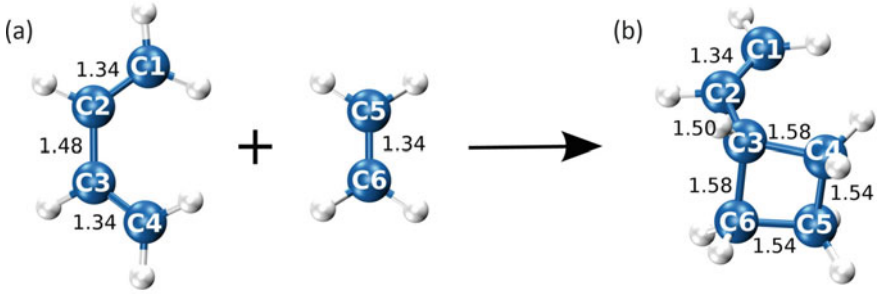

Fig. 2.15 Optimized structures of **a** reactants (butadiene and ethylene) and **b** product (vinylcyclobutane) for the side reaction between butadiene and ethylene in the absence of external pressure. Reprinted (adapted) from [2], with the permission of AIP publishing

pathway via the anti-diradical. Effects of compression were not studied, because, at even the smallest compressive pressures used (P_{HP} = −0.31 kcal mol^{-1}Å^{-2}), the gauche-diradical spontaneously transitioned into vinylcyclobutane.

2.3.4.3 Side Reaction: Formation of Vinylcyclobutane

Experimentally, vinylcyclobutane is produced in a side reaction when the parent DA reaction is being carried out [122], as we have observed in our calculations under compression, and therefore, we examined the side reaction mechanisms and the modifications produced by compressive pressure.

Figure 2.15 shows the optimized geometries and bond lengths (in Å) of the reactants (butadiene and ethylene) and the product (vinylcyclobutane) on the unmodified PES. The energies along the reaction coordinate as a function of compression, P_{HP}, for the reaction of butadiene + ethylene → vinylcyclobutane are shown in Fig. 2.16. For some values of $P_{HP} \neq 0$, a kink in the reaction pathway was seen. These kinks were present at a range of spring constants that spanned an order of magnitude. The activation energies, summarized in Table 2.8, are non-monotonic behavior with com-

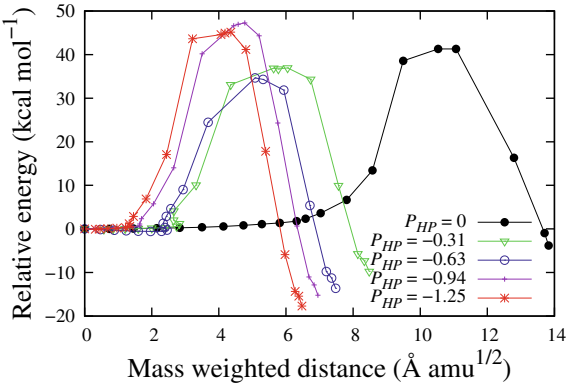

Fig. 2.16 Energy along the reaction coordinate for the side reaction that results in the formation of vinylcyclobutane, as a function of pseudo-hydrostatic pressures, P_{HP} (in kcal mol^{-1} Å^{-2}), indicated in the legend. The energies of the reactants (butadiene + ethylene) are shifted to zero in all cases. The vibrational ZPE correction has not been included in this plot. Reprinted (adapted) from [2], with the permission of AIP publishing

pression. At $P_{HP} = 0$, the energy barrier for this transition is 42.4 kcal mol^{-1}, and the reaction is slightly endothermic (by 2 kcal mol^{-1}). As the reaction proceeds, butadiene and ethylene approach each other, and yield vinylcyclobutane. The order in which these bonds form was observed to depend on the magnitude of the compressive pressure, and gives rise to different pathways. For lower compression ($-0.63 \leq P_{HP} \leq 0$ kcal mol^{-1} Å^{-2}), the optimized structures along the reaction path indicated the formation of C4−C5 bonds (see Fig. 2.15b) form first, followed by the C3−C6, and therefore the barrier decreases, suggesting that the increasing compression facilitates this process. On the other hand, higher compression ($P_{HP} \leq -0.94$ kcal mol^{-1} Å^{-2}) results in the formation of C3−C6 first, followed by C4−C5, and this pathway appears to present a higher barrier, therefore the barrier increases at $P_{HP} = -0.94$ kcal mol^{-1} Å^{-2}, however further increasing compression resulted in the decrease in the barrier by facilitating the side reaction. This switching of the order of bond formation seems to lead to the non-monotonic behavior of the energy barrier with compression.

2.4 Conclusions

In this chapter, we described a method for studying the influence of external forces on the Born-Oppenheimer potential energy surface (PES) of atomic systems, and demonstrated its applications by calculating reaction pathways for various reactions under the influence of external forces. This was done using a formulation for computing energies on a generalized force-modified potential energy surface (G-FMPES), and demonstrated that calculation of atomistic quantities (including transition states)

Table 2.8 Activation (E_a) and reaction (E_{rxn}) energies for butadiene + ethylene → vinylcyclobutane reaction as a function of pseudo-hydrostatic pressure, P_{HP} (in kcal mol^{-1} Å^{-2}), calculated using CASSCF(6,6) level of theory

P_{HP}	E_a	E_{rxn}
0	42.4	+2.0
−0.31	38.1	−4.0
−0.63	35.8	−7.8
−0.94	48.4	−9.4
−1.25	46.3	−11.9

The positive value of E_{rxn} implies the reaction is endothermic. All energies are expressed in kcal mol^{-1} Adapted from [2]

in the presence of a spatially varying force is easily accomplished using standard atomistic techniques. We have exemplified the formulation by calculating a variety of atomistic properties for (i) conformational transitions in ethane and RDX molecules, (ii) the decomposition of RDX, and (iii) the reaction between 1,3-butadiene and ethylene. For various transitions, we showed that the curvature of the G-FMPES is indeed different from that of the unmodified PES, and that it has an effect on the harmonic transition rates. Also seen were examples where the addition of an external pressure causes a state to become unstable, indicating the merging of a saddle point with the energy minimum, as a result of the increasing compressive pressures enhancing steric effects by forcing molecules into more compact conformations. For both the ethane and RDX molecules, increasing compressive pressures shifted the vibrational spectra toward stiffer mode: a behavior that is qualitatively consistent with independent experiments, as well as molecular dynamics studies. Our study of the parent Diels-Alder reaction between butadiene and ethylene indicated that the activation energy barrier of this reaction decreases with increasing compressive pressure. We also observed that one reaction pathway, the formation of cyclohexene by the gauche-diradical pathway, become inaccessible due to the compressive pressures. At sufficiently high compression, the barrier of the concerted pathway becomes zero and the reaction becomes spontaneous. Our estimates indicated that the compression used in our Diels-Alder reaction corresponds to a range of 68 MPa to 1410 MPa. This range can be accessed in laboratories by using shock-wave technologies or diamond-anvil cells, in order to test the predictions made in this work [61, 125].

Appendix 1: Proof that the external force field is conservative

For a 3-dimensional, N-atom system, the position vector of the jth atom, and the external force vector on it are given in component form as

$$\mathbf{r}^{(j)} = \left(x^{(j)}, y^{(j)}, z^{(j)}\right) \tag{2.14}$$

$$\mathbf{f}_{\text{ext}}^{(j)} = \left(f_{\text{ext},x}^{(j)}, f_{\text{ext},y}^{(j)}, f_{\text{ext},z}^{(j)}\right) \tag{2.15}$$

where various $\left\{\mathbf{f}_{\text{ext}}^{(j)}\ \forall\ j = 1, 2, 3 \ldots N\right\}$ make up the external force field $\mathbf{F}_{\text{ext}}(\mathbf{R})$.

Geometric centroid of the configuration is given by the mean position of all the atoms in the configuration as

$$\mathbf{c} = \left(c_x, c_y, c_z\right) = \left(\left\langle x^{(j)}\right\rangle, \left\langle y^{(j)}\right\rangle, \left\langle z^{(j)}\right\rangle\right) \tag{2.16}$$

where $\langle\cdot\rangle$ denotes an average taken over all N atoms.

According to our prescription of pseudo-hydrostatic pressure, external force on the jth atom is given as

$$\mathbf{f}_{\text{ext}}^{(j)} = P_{HP}\left[\mathbf{r}^{(j)} - \mathbf{c}\right]; \quad \forall \quad j = 1, 2, 3 \ldots N \tag{2.17}$$

where P_{HP} is a user-defined "pressure."

First derivatives of the external force vector are given by

$$\left\{\frac{\partial \mathbf{f}_{\text{ext}}^{(j)}}{\partial x^{(k)}}, \frac{\partial \mathbf{f}_{\text{ext}}^{(j)}}{\partial y^{(k)}}, \frac{\partial \mathbf{f}_{\text{ext}}^{(j)}}{\partial z^{(k)}}; \quad \forall \quad j, k = 1, 2, 3 \ldots N\right\} \tag{2.18}$$

The first of this set is

$$\frac{\partial \mathbf{f}_{\text{ext}}^{(j)}}{\partial x^{(k)}} = P_{HP}\left(\frac{\partial \mathbf{r}^{(j)}}{\partial x^{(k)}} - \frac{\partial \mathbf{c}}{\partial x^{(k)}}\right) \tag{2.19}$$

with

$$\frac{\partial \mathbf{r}^{(j)}}{\partial x^{(k)}} = \left(\frac{\partial x^{(j)}}{\partial x^{(k)}}, \frac{\partial y^{(j)}}{\partial x^{(k)}}, \frac{\partial z^{(j)}}{\partial x^{(k)}}\right) = \left(\delta_{jk}, 0, 0\right) \tag{2.20}$$

$$\frac{\partial \mathbf{c}}{\partial x^{(k)}} = \left(\frac{\partial \langle x\rangle}{\partial x^{(k)}}, \frac{\partial \langle y\rangle}{\partial x^{(k)}}, \frac{\partial \langle z\rangle}{\partial x^{(k)}}\right) = \left(\frac{1}{N}, 0, 0\right) \tag{2.21}$$

where δ_{jk} is the Kronecker delta. Using this, and similar results for the other derivatives, first derivatives of the external force vector are

$$\frac{\partial \mathbf{f}_{\text{ext}}^{(j)}}{\partial x^{(k)}} = P_{HP}\left(\delta_{jk} - \frac{1}{N}, 0, 0\right) \tag{2.22}$$

$$\frac{\partial \mathbf{f}_{\text{ext}}^{(j)}}{\partial y^{(k)}} = P_{HP}\left(0, \delta_{jk} - \frac{1}{N}, 0\right) \tag{2.23}$$

$$\frac{\partial \mathbf{f}_{\text{ext}}^{(j)}}{\partial z^{(k)}} = P_{HP}\left(0, 0, \delta_{jk} - \frac{1}{N}\right) \tag{2.24}$$

which are all constant for all values of j and k and therefore exist and are continuous everywhere, proving that the external force field is conservative.

Appendix 2: The NEB method on a G-FMPES

With the understanding of how to compute energies, forces, and curvatures on a G-FMPES, the NEB implementation for finding MEPs on a G-FMPES closely follows the original implementation, but with a few crucial modifications. For clarity, our implementation of a G-FMPES is outlined below.

The start and end point structures are re-optimized with the external force and a set of images is initialized between them. Consecutive images are connected by harmonic springs with an equilibrium length of zero and a user-specified spring stiffness k_{spring} (the actual value of which is not particularly important as long as it is greater than zero, but needs to be on the order of the system forces for efficient convergence). The band is iteratively optimized until the net force on each image is minimized to within a user-specified tolerance. At each iteration, the net force on the i^{th} image located at $\mathbf{R}^{(i)}$ on the G-FMPES is given by the projected (nudged) forces as:

$$\overline{\mathbf{F}}^{(i)}_{\text{net,nudged}} = \left[\mathbf{F}^{(i)}_{\text{grad}} + \mathbf{F}^{(i)}_{\text{ext}}\right]_{\perp} + \left[\mathbf{F}^{(i)}_{\text{spring}}\right]_{\parallel} \tag{2.25}$$

where the subscript $\perp$ (or $\parallel$) on a vector indicates its component perpendicular (or parallel) to the unit tangent $\hat{\boldsymbol{\tau}}^{(i)}$. The un-normalized tangent $\boldsymbol{\tau}^{(i)}$ is computed using Henkelman and Jónsson's improved tangent estimate [50]. Defining

$$\boldsymbol{\tau}^{(i)+} = \mathbf{R}^{(i+1)} - \mathbf{R}^{(i)} \tag{2.26}$$

$$\boldsymbol{\tau}^{(i)-} = \mathbf{R}^{(i)} - \mathbf{R}^{(i-1)} \tag{2.27}$$

the tangent is estimated as

$$\boldsymbol{\tau}^{(i)} = \begin{cases} \boldsymbol{\tau}^{(i)+} & \text{if} \quad \overline{V}^{(i+1)} > \overline{V}^{(i)} > \overline{V}^{(i-1)} \\ \boldsymbol{\tau}^{(i)-} & \text{if} \quad \overline{V}^{(i+1)} < \overline{V}^{(i)} < \overline{V}^{(i-1)} \end{cases} \tag{2.28}$$

where the different $\overline{V}$ are computed using the line integral, as defined in the main article. In the event that the three consecutive values of $\overline{V}$ are neither strictly increasing nor strictly decreasing, i.e., if $\overline{V}^{(i+1)} \leq \overline{V}^{(i)} \geq \overline{V}^{(i-1)}$ or $\overline{V}^{(i+1)} \geq \overline{V}^{(i)} \leq \overline{V}^{(i-1)}$, in order to prevent abrupt switching between two possible tangents, the tangent is taken to be a weighted average as

$$\boldsymbol{\tau}^{(i)} = \begin{cases} \boldsymbol{\tau}^{(i)+}\Delta\overline{V}^{(i)+} + \boldsymbol{\tau}^{(i)-}\Delta\overline{V}^{(i)-} & \text{if} \quad \overline{V}^{(i+1)} > \overline{V}^{(i-1)} \\ \boldsymbol{\tau}^{(i)+}\Delta\overline{V}^{(i)-} + \boldsymbol{\tau}^{(i)-}\Delta\overline{V}^{(i)+} & \text{if} \quad \overline{V}^{(i+1)} < \overline{V}^{(i-1)} \end{cases} \tag{2.29}$$

with

$$\Delta\overline{V}^{(i)+} = \max\left(\left|\overline{V}^{(i+1)} - \overline{V}^{(i)}\right|, \left|\overline{V}^{(i-1)} - \overline{V}^{(i)}\right|\right) \tag{2.30}$$

$$\Delta\overline{V}^{(i)-} = \min\left(\left|\overline{V}^{(i+1)} - \overline{V}^{(i)}\right|, \left|\overline{V}^{(i-1)} - \overline{V}^{(i)}\right| \right) \tag{2.31}$$

The component of the spring force parallel to the tangent is computed as

$$\left[\mathbf{F}^{(i)}_{\text{spring}}\right]_{\parallel} = k_{\text{spring}} \left(\left\|\boldsymbol{\tau}^{(i)+}\right\| - \left\|\boldsymbol{\tau}^{(i)-}\right\| \right) \hat{\boldsymbol{\tau}}^{(i)} \tag{2.32}$$

At each iteration, the climbing-image method [51] is applied to the highest energy image along the band. This image, identified by $i = h$, is free from all spring forces and is assigned a climbing force computed by inverting the component of the gradient plus external forces along the tangent to this image which is expressed as

$$\overline{\mathbf{F}}^{(i)}_{\text{net,climb}} = \left(\mathbf{F}^{(i)}_{\text{grad}} + \mathbf{F}^{(i)}_{\text{ext}}\right) - 2\left[\left(\mathbf{F}^{(i)}_{\text{grad}} + \mathbf{F}^{(i)}_{\text{ext}}\right) \cdot \hat{\boldsymbol{\tau}}^{(i)}\right] \hat{\boldsymbol{\tau}}^{(i)} \tag{2.33}$$

and makes the highest image move uphill along the direction of the first eigenvector, and downhill along all other directions.

In the more recent variation with two climbing images [52], the highest image (with $i = h$) is not allowed to climb but is nudged in the usual manner by assigning its net force to be equal to $\overline{\mathbf{F}}_{\text{net,nudged}}$ as in Eq. (2.25). However, its two nearest neighbors (one from each side of the band, i.e., images with $i = h \pm 1$) are assigned climbing forces as in Eq. (2.33). This prescription results in a higher density of images near the saddle point and is particularly useful for MEPs with unusually high curvatures near the saddle point which would cause the NEB tangent direction to be different from the MEP tangent direction.

Having computed the net force on each image, the band is iteratively optimized until it is well-converged by moving each image toward the point of minimum net force using a suitable optimizer.

References

1. Subramanian G, Mathew N, Leiding J (2015) A generalized force-modified potential energy surface for mechanochemical simulations. J Chem Phys 143(13):134109
2. Jha SK, Brown K, Todde G, Subramanian G (2016) A mechanochemical study of the effects of compression on a diels-alder reaction. J Chem Phys 145(7):074307
3. Todde G, Jha SK, Subramanian G (2017) The effect of external forces on the initial dissociation of rdx (1,3,5-trinitro-1,3,5-triazine): a mechanochemical study. Int J Quantum Chem 117(20):e25426
4. Varvenne C, Bruneval F, Marinica M-C, Clouet E (2013) Point defect modeling in materials: coupling ab initio and elasticity approaches. Phys Rev B 88(13):134102
5. Clouet E, Garruchet S, Nguyen H, Perez M, Becquart CS (2008) Dislocation interaction with c in α-fe: a comparison between atomic simulations and elasticity theory. Acta Mater 56(14):3450–3460

6. Ong MT, Leiding J, Tao H, Virshup AM, Martínez TJ (2009) First principles dynamics and minimum energy pathways for mechanochemical ring opening of cyclobutene. J Am Chem Soc 131(18):6377–6379
7. Konda SSM, Brantley JN, Varghese BT, Wiggins KM, Bielawski CW, Makarov DE (2013) Molecular catch bonds and the anti-Hammond effect in polymer mechanochemistry. J Am Chem Soc 135(34):12722–12729
8. Wang J, Kouznetsova TB, Niu Z, Ong MT, Klukovich HM, Rheingold AL, Martinez TJ, Craig SL (2015) Inducing and quantifying forbidden reactivity with single-molecule polymer mechanochemistry. Nat Chem 7(4):323–327
9. Konda SSM, Avdoshenko SM, Makarov DE (2014) Exploring the topography of the stress-modified energy landscapes of mechanosensitive molecules. J Chem Phys 140(10):104114
10. Silberstein MN, Min K, Cremar LD, Degen CM, Martinez TJ, Aluru NR, White SR, Sottos NR (2013) Modeling mechanophore activation within a crosslinked glassy matrix. J Appl Phys 114(2):023504
11. Silberstein MN, Cremar LD, Beiermann BA, Kramer SB, Martinez TJ, White SR, Sottos NR (2014) Modeling mechanophore activation within a viscous rubbery network. J Mech Phys Solids 63:141–153
12. Bailey A, Mosey NJ (2012) Prediction of reaction barriers and force-induced instabilities under mechanochemical conditions with an approximate model: a case study of the ring opening of 1, 3-cyclohexadiene. J Chem Phys 136(4):01B613
13. Kumamoto K, Fukada I, Kotsuki H (2004) Diels–alder reaction of thiophene: dramatic effects of high-pressure/solvent-free conditions. Angew Chem Int Ed 43(15):2015–2017
14. Mianowski A, Robak Z, Tomaszewicz M, Stelmach S (2012) The boudouard-bell reaction analysis under high pressure conditions. J Therm Anal Calorim 110(1):93–102
15. Kiselev VD (2013) High-pressure influence on the rate of diels–alder cycloaddition reactions of maleic anhydride with some dienes. Int J Chem Kinet 45(9):613–622
16. Kiselev VD, Kornilov DA, Kashaeva EA, Potapova LN, Konovalov AI (2014) Effect of pressure on the rate of the diels-alder reaction of diethyl azodicarboxylate with 9, 10-dimethylanthracene. Russ J Org Chem 50(4):489–493
17. McMillan PF (2002) New materials from high-pressure experiments. Nat Mater 1(1):19–25
18. Gillet P, Badro J, Varrel B, McMillan PF (1995) High-pressure behavior in α-alpo 4: amorphization and the memory-glass effect. Phys Rev B 51(17):11262
19. J Torres A, Serment-Moreno V, Escobedo-Avellaneda ZJ, Velazquez G, Welti-Chanes J (2016) Reaction chemistry at high pressure and high temperature. In: High pressure processing of food. Springer, pp 461–478
20. Hashemi H, Christensen JM, Gersen S, Glarborg P (2015) Hydrogen oxidation at high pressure and intermediate temperatures: experiments and kinetic modeling. Proc Combust Inst 35(1):553–560
21. Ribas-Arino J, Shiga M, Marx D (2009) Understanding covalent mechanochemistry. Angew Chem Int Ed 48(23):4190–4193
22. Ribas-Arino J, Marx D (2012) Covalent mechanochemistry: theoretical concepts and computational tools with applications to molecular nanomechanics. Chem Rev 112(10):5412–5487
23. Lenhardt JM, Ong MT, Choe R, Evenhuis CR, Martinez TJ, Craig SL (2010) Trapping a diradical transition state by mechanochemical polymer extension. Science 329(5995):1057–1060
24. Kochhar GS, Bailey A, Mosey NJ (2010) Competition between orbitals and stress in mechanochemistry. Angew Chem Int Ed 49(41):7452–7455
25. Smalø HS, Rybkin VV, Klopper W, Helgaker T, Uggerud E (2014) Mechanochemistry: the effect of dynamics. J Phys Chem A 118(36):7683–7694
26. Avdoshenko SM, Makarov DE (2015) Finding mechanochemical pathways and barriers without transition state search. J Chem Phys 142(17):174106
27. Wang J, Kouznetsova TB, Craig SL (2015) Reactivity and mechanism of a mechanically activated anti-woodward–hoffmann–depuy reaction. J Am Chem Soc 137(36):11554–11557

28. Makarov DE (2016) Perspective: mechanochemistry of biological and synthetic molecules. J Chem Phys 144(3):030901
29. Subramanian G, Perez D, Uberuaga BP, Tomé CN, Voter AF (2013) Method to account for arbitrary strains in kinetic Monte Carlo simulations. Phys Rev B 87:144107
30. Goyal A, Phillpot SR, Subramanian G, Andersson DA, Stanek CR, Uberuaga Blas P (2015) Impact of homogeneous strain on uranium vacancy diffusion in uranium dioxide. Phys Rev B 91:094103
31. Vérité G, Domain C, Fu C-C, Gasca P, Legris A, Willaime F (2013) Self-interstitial defects in hexagonal close packed metals revisited: evidence for low-symmetry configurations in Ti, Zr, and Hf. Phys Rev B 87(13):134108
32. Garnier T, Manga VR, Bellon P, Trinkle DR (2014) Diffusion of Si impurities in Ni under stress: a first-principles study. Phys Rev B 90:024306
33. Mathew N, Picu RC (2011) Molecular conformational stability in cyclotrimethylene trinitramine crystals. J Chem Phys 135(2):024510
34. Munday LB, Chung PW, Rice BM, Solares SD (2011) Simulations of high-pressure phases in RDX. J Phys Chem B 115(15):4378–4386
35. Cawkwell MJ, Sewell TD, Zheng L, Thompson DL (2008) Shock-induced shear bands in an energetic molecular crystal: application of shock-front absorbing boundary conditions to molecular dynamics simulations. Phys Rev B 78(1):014107
36. Boyd S, Murray JS, Politzer P (2009) Molecular dynamics characterization of void defects in crystalline (1, 3, 5-trinitro-1, 3, 5-triazacyclohexane). J Chem Phys 131(20):204903
37. Ramos KJ, Hooks DE, Sewell TD, Cawkwell MJ (2010) Anomalous hardening under shock compression in (021)-oriented cyclotrimethylene trinitramine single crystals. J Appl Phys 108(6):066105
38. Munday LB, Solares SD, Chung PW (2012) Generalized stacking fault energy surfaces in the molecular crystal αRDX. Philos Mag 92(24):3036–3050
39. Mathew N, Picu CR, Chung PW (2013) Peierls stress of dislocations in molecular crystal cyclotrimethylene trinitramine. J Phys Chem A 117(25):5326–5334
40. Pal A, Picu RC (2014) Rotational defects in cyclotrimethylene trinitramine (rdx) crystals. J Chem Phys 140(4):044512
41. Austin DE, Peng Y, Hansen BJ, Miller IW, Rockwood AL, Hawkins AR, Tolley SE (2008) Novel ion traps using planar resistive electrodes: implications for miniaturized mass analyzers. J Am Soc Mass Spectrom 19(10):1435–1441
42. Dudko OK, Hummer G, Szabo A (2008) Theory, analysis, and interpretation of single-molecule force spectroscopy experiments. Proc Natl Acad Sci USA 105(41):15755–15760
43. Neuman KC, Nagy A (2008) Single-molecule force spectroscopy: optical tweezers, magnetic tweezers and atomic force microscopy. Nat Methods 5(6):491–505
44. Kochhar GS, Heverly-Coulson GS, Mosey NJ (2015) Theoretical approaches for understanding the interplay between stress and chemical reactivity. In: Polymer mechanochemistry. Springer, pp 37–96
45. Stauch T, Dreuw A (2016) Advances in quantum mechanochemistry: electronic structure methods and force analysis. Chem Rev 116(22):14137–14180
46. Henkelman G, Jóhannesson G, Jónsson H (2002) Methods for finding saddle points and minimum energy paths. In: Theoretical methods in condensed phase chemistry, vol 5. Springer, pp 269–302
47. Uberuaga BP, Hoagland RG, Voter AF, Valone SM (2007) Direct transformation of vacancy voids to stacking fault tetrahedra. Phys Rev Lett 99(13):135501
48. Vineyard GH (1957) Frequency factors and isotope effects in solid state rate processes. J Phys Chem Solids 3(1-2):121–127
49. Werner H-JKPJ, Knowles PJ, Knizia G, Manby FR, Schütz M, Celani P, Korona T, Lindh R, Mitrushenkov A, Rauhut G et al (2012) Molpro, version 2012.1, a package of ab initio programs. see http://www.molpro.net
50. Henkelman G, Jónsson H (2000) Improved tangent estimate in the nudged elastic band method for finding minimum energy paths and saddle points. J Chem Phys 113(22):9978–9985

51. Henkelman G, Uberuaga BP, Jónsson H (2000) A climbing image nudged elastic band method for finding saddle points and minimum energy paths. J Chem Phys 113(22):9901–9904
52. Zarkevich NA, Johnson DD (2015) Nudged-elastic band method with two climbing images: finding transition states in complex energy landscapes. J Chem Phys 142(2):024106
53. Bitzek E, Koskinen P, Gähler F, Moseler M, Gumbsch P (2006) Structural relaxation made simple. Phys Rev Lett 97:170201
54. Hartree DR (1928) The wave mechanics of an atom with a non-coulomb central field. Part I. theory and methods. In: Mathematics proceedings Cambridge, vol 24. Cambridge University Press, pp 89–110
55. Fock V (1930) Näherungsmethode zur lösung des quantenmechanischen mehrkörperproblems. Zeitschrift für Physik 61(1–2):126–148
56. Slater JC (1930) Note on Hartree's method. Phys Rev 35:210–211
57. Krishnan R, Binkley JS, Seeger R, Pople JA (1980) Self-consistent molecular orbital methods. xx. A basis set for correlated wave functions. J Chem Phys 72(1):650–654
58. Kemp JD, Pitzer KS (1936) Hindered rotation of the methyl groups in ethane. J Chem Phys 4(11):749–749
59. Eyring H, Grant DM, Hecht H (1962) The rotational barrier in ethane. J Chem Educ 39(9):466
60. Johnson RD III (ed) (2013) NIST computational chemistry comparison and benchmark database, NIST standard reference database number 101, release 16a, august 2013. see http://cccbdb.nist.gov/
61. Kurnosov AV, Ogienko AG, Goryainov SV, Larionov EG, Manakov AY, Lihacheva AY, Aladko EY, Zhurko FV, Voronin VI, Berger IF et al (2006) Phase diagram and high-pressure boundary of hydrate formation in the ethane- water system. J Phys Chem B 110(43):21788–21792
62. Cawkwell MJ, Ramos KJ, Hooks DE, Sewell TD (2010) Homogeneous dislocation nucleation in cyclotrimethylene trinitramine under shock loading. J Appl Phys 107(6):063512
63. Mathew N, Picu RC (2013) Slip asymmetry in the molecular crystal cyclotrimethylenetrinitramine. Chem Phys Lett 582:78–81
64. Munday LB, Mitchell RL, Knap J, Chung PW (2013) Role of molecule flexibility on the nucleation of dislocations in molecular crystals. Appl Phys Lett 103(15):151911
65. Rice BM, Chabalowski CF (1997) Ab initio and nonlocal density functional study of 1, 3, 5-trinitro-s-triazine (RDX) conformers. J Phys Chem A 101(46):8720–8726
66. Karpowicz RJ, Brill TB (1984) Comparison of the molecular structure of hexahydro-1, 3, 5-trinitro-s-triazine in the vapor, solution and solid phases. J Phys Chem 88(3):348–352
67. Davidson AJ, Oswald IDH, Francis DJ, Lennie AR, Marshall WG, Millar DIA, Pulham CR, Warren JE, Cumming AS (2008) Explosives under pressure-the crystal structure of γ-RDX as determined by high-pressure x-ray and neutron diffraction. Cryst Eng Comm 10(2):162–165
68. Millar DIA, Oswald IDH, Barry C, Francis DJ, Marshall WG, Pulham CR, Cumming AS (2010) Pressure-cooking of explosives-the crystal structure of ε-RDX as determined by x-ray and neutron diffraction. Chem Commun 46:5662–5664
69. Dreger ZA, Gupta YM (2010) Raman spectroscopy of high-pressure- high-temperature polymorph of hexahydro-1, 3, 5-trinitro-1, 3, 5-triazine (ε-RDX). J Phys Chem A 114(26):7038–7047
70. Zheng X, Zhao J, Tan D, Liu C, Song Y, Yang Yanqiang (2011) High-pressure vibrational spectroscopy of hexahydro-1, 3, 5-trinitro-1, 3, 5-triazine (RDX). Propellants Explos Pyrotech 36(1):22–27
71. Ciezak JA, Jenkins TA, Liu Z, Hemley RJ (2007) High-pressure vibrational spectroscopy of energetic materials: hexahydro-1, 3, 5-trinitro-1, 3, 5-triazine. J Phys Chem A 111(1):59–63
72. Pereverzev A, Sewell TD, Thompson DL (2013) Molecular dynamics study of the pressure-dependent terahertz infrared absorption spectrum of α-and γ-RDX. J Chem Phys 139(4):044108
73. Chakraborty D, Muller RP, Dasgupta S, Goddard WA (2000) The mechanism for unimolecular decomposition of rdx (1, 3, 5-trinitro-1, 3, 5-triazine), an ab initio study. J Phys Chem A 104(11):2261–2272

74. Harris NJ, Lammertsma K (1997) Ab initio density functional computations of conformations and bond dissociation energies for hexahydro-1, 3, 5-trinitro-1, 3, 5-triazine. J Am Chem Soc 119(28):6583–6589
75. Shishkov IF, Vilkov LV, Kolonits M, Rozsondai B (1991) The molecular geometries of some cyclic nitramines in the gas phase. Struct Chem 2(1):57–64
76. Chakraborty D, Muller RP, Dasgupta S, Goddard WA (2001) A detailed model for the decomposition of nitramines: RDX and HMX. J Comput Aided Mater 8(2-3):203–212
77. Schweigert IV (2015) Ab initio molecular dynamics of high-temperature unimolecular dissociation of gas-phase RDX and its dissociation products. J Phys Chem A 119(12):2747–2759
78. Wu CJ, Fried LE (1997) Ab initio study of RDX decomposition mechanisms. J Phys Chem A 101(46):8675–8679
79. Molt RW, Watson T, Bazanté AP, Bartlett RJ, Richards NGJ (2016) Gas phase RDX decomposition pathways using coupled cluster theory. Phys Chem Chem Phys 18(37):26069–26077
80. Diels O, Alder K (1928) Syntheses in the hydroaromatic series. I. addition of "diene" hydrocarbons. Justus Liebigs Ann Chem 460:98–122
81. Carruthers W (1978) Some Mod Methods Org Synth, 2nd edn. Cambridge University Press, Cambridge
82. Cycloaddition reactions in organic synthesis. Pergamon Press, Oxford (1990)
83. Boger DL, Weinberg SN (1987) Hetero-Diels methodology in organic synthesis. Academic Press Inc, San Diego
84. Houk KN, Gonzalez J, Li Y (1995) Pericyclic reaction transition states: passions and punctilios, 1935-1995. Acc Chem Res 28(2):81–90
85. Lee GY, Kim HY, Han IS (1999) DFT studies of the diels-alder reaction of 1, 4-diaza-1, 3-butadiene with acrolein. Korean Chem Soc 20(5):621–623
86. Domingo LR, Andrés J (2003) Enhancing reactivity of carbonyl compounds via hydrogen-bond formation. A DFT study of the hetero-diels- alder reaction between butadiene derivative and acetone in chloroform. J Org Chem 68(22):8662–8668
87. Zhang X, Haifeng D, Wang Z, Yun-Dong W, Ding K (2006) Experimental and theoretical studies on the hydrogen-bond-promoted enantioselective hetero-diels-alder reaction of danishefsky's diene with benzaldehyde. J Org Chem 71(7):2862–2869
88. Akiyama T, Morita H, Fuchibe K (2006) Chiral brønsted acid-catalyzed inverse electron-demand AZA diels-alder reaction. J Am Chem Soc 128(40):13070–13071
89. Esquivias J, Arrayás RG, Carretero JC (2007) Catalytic asymmetric inverse-electron-demand diels- alder reaction of n-sulfonyl-1-AZA-1, 3-dienes. J Am Chem Soc 129(6):1480–1481
90. Liu D, Canales E, Corey EJ (2007) Chiral oxazaborolidine- aluminum bromide complexes are unusually powerful and effective catalysts for enantioselective diels-alder reactions. J Am Chem Soc 129(6):1498–1499
91. Domingo LR, Sáez JA (2009) Understanding the mechanism of polar diels-alder reactions. Org Biomol Chem 7(17):3576–3583
92. Jiang H, Cruz DC, Li Y, Lauridsen VH, Jørgensen KA (2013) Asymmetric organocatalytic thio-diels–alder reactions via trienamine catalysis. J Am Chem Soc 135(13):5200–5207
93. Sato S, Maeda Y, Guo J-D, Yamada M, Mizorogi N, Nagase Shigeru, Akasaka Takeshi (2013) Mechanistic study of the diels-alder reaction of paramagnetic endohedral metallofullerene: reaction of la@ c82 with 1, 2, 3, 4, 5-pentamethylcyclopentadiene. J Am Chem Soc 135(15):5582–5587
94. Yuan C, Biao D, Yang L, Liu B (2013) Bioinspired total synthesis of bolivianine: a diels-alder/intramolecular hetero-diels-alder cascade approach. J Am Chem Soc 135(25):9291–9294
95. Dell'Amico L, Vega-Peñaloza A, Cuadros S, Melchiorre P (2016) Enantioselective organocatalytic diels–alder trapping of photochemically generated hydroxy-o-quinodimethanes. Angew Chem Int Ed 55(10):3313–3317
96. Andrews DR, Barton DHR, Hesse RH, Pechet MM (1986) Synthesis of 25-hydroxy-and 1. alpha., 25-dihydroxy vitamin d3 from vitamin d2 (calciferol). J Org Chem 51(25):4819–4828

97. Lygo B, Bhatia M, Cooke JWB, Hirst DJ (2003) Synthesis of (±)-solanapyrones a and b. Tetrahedron Lett 44(12):2529–2532
98. Burns AC, Forsyth CJ (2008) Intramolecular diels-alder/Tsuji allylation assembly of the functionalized trans-decalin of salvinorin A. Org Lett 10(1):97–100
99. Chackalamannil S, Davies RJ, Wang Y, Asberom T, Doller D, Wong J, Leone D, McPhail AT (1999) Total synthesis of (+)-himbacine and (+)-himbeline. J Org Chem 64(6):1932–1940
100. Funel JA, Abele S (2013) Industrial applications of the diels–alder reaction. Angew Chem Int Ed 52(14):3822–3863
101. Roos BO (1987) The complete active space self-consistent field method and its applications in electronic structure calculations. Adv Chem Phys 69:399–445
102. Roos BO (1980) The complete active space SCF method in a fock-matrix-based super-ci formulation. Int J Quantum Chem Symp 18(S14):175–189
103. Bernardi F, Bottoni A, Field MJ, Guest MF, Hillier IH, Robb MA, Venturini A (1988) MC-SCF study of the diels-alder reaction between ethylene and butadiene. J Am Chem Soc 110(10):3050–3055
104. Wiest O, Montiel DC, Houk KN (1997) Quantum mechanical methods and the interpretation and prediction of pericyclic reaction mechanisms. J Phys Chem A 101(45):8378–8388
105. Goldstein E, Beno B, Houk KN (1996) Density functional theory prediction of the relative energies and isotope effects for the concerted and stepwise mechanisms of the diels-alder reaction of butadiene and ethylene. J Am Chem Soc 118(25):6036–6043
106. Goodrow A, Bell AT, Head-Gordon M (2009) Transition state-finding strategies for use with the growing string method. J Chem Phys 130(24):244108
107. Rowley D, Steiner H (1951) Kinetics of diene reactions at high temperatures. Discuss Faraday Soc 10:198–213
108. Evans MG (1939) The activation energies of reactions involving conjugated systems. Trans Faraday Soc 35:824–834
109. Robert Burns Woodward and Roald Hoffmann (1969) The conservation of orbital symmetry. Angew Chem Int Ed 8(11):781–853
110. Dewar MJ, Griffin AC, Kirschner S (1974) Mindo/3 study of some diels-alder reactions. J Am Chem Soc 96(19):6225–6226
111. Dewar MJS, Olivella S, Rzepa HS (1978) Ground states of molecules. 49. mindo/3 study of the retro-diels-alder reaction of cyclohexene. J Am Chem Soc 100(18):5650–5659
112. Frey HM, Pottinger R (1978) Thermal unimolecular reactions of vinylcyclobutane and isopropenylcyclobutane. J Chem Soc Faraday Trans 1 74:1827–1833
113. Dewar MJS, Pierini AB (1984) Mechanism of the diels-alder reaction. studies of the addition of maleic anhydride to furan and methylfurans. J Am Chem Soc 106(1):203–208
114. Dewar MJS (1984) Multibond reactions cannot normally be synchronous. J Am Chem Soc 106(1):209–219
115. Dewar MJS, Olivella S, Stewart JJP (1986) Mechanism of the diels-alder reaction: reactions of butadiene with ethylene and cyanoethylenes. J Am Chem Soc 108(19):5771–5779
116. Houk KN, Lin YT, Brown FK (1986) Evidence for the concerted mechanism of the diels-alder reaction of butadiene with ethylene. J Am Chem Soc 108(3):554–556
117. Dewar MJS, Jie C (1992) Mechanisms of pericyclic reactions: the role of quantitative theory in the study of reaction mechanisms. Acc Chem Res 25(11):537–543
118. Townshend RE, Ramunni G, Segal G, Hehre WJ, Salem L (1976) Organic transition states. V. the diels-alder reaction. J Am Chem Soc 98(8):2190–2198
119. Sakai S (2000) Theoretical analysis of concerted and stepwise mechanisms of diels-alder reaction between butadiene and ethylene. J Phys Chem A 104(5):922–927
120. Cui C-X, Liu Y-J (2014) A thorough understanding of the diels-alder reaction of 1, 3-butadiene and ethylene. J Phys Org Chem 27(8):652–660
121. Li Y, Houk KN (1993) Diels-alder dimerization of 1, 3-butadiene: an ab initio CASSCF study of the concerted and stepwise mechanisms and butadiene-ethylene revisited. J Am Chem Soc 115(16):7478–7485

122. Bartlett PD, Schueller KE (1968) Cycloaddition. VIII. ethylene as a dienophile. a minute amount of 1, 2-cycloaddition of ethylene to butadiene. J Am Chem Soc 90(22):6071–6077
123. Lide DR (eds) (2009) CRC handbook of chemistry and physics, 89th edn. CRC/Taylor & Francis, Boca Raton, FL
124. Bell GI (1978) Models for the specific adhesion of cells to cells. Science 200(4342):618–627
125. Ivanov AN, Litvin DF, Savenko BN, Smirnov LS, Voronin VI, Teplykh AE (1995) High pressure cell for neutron diffraction investigations. High Pressure Res 14(1–3):209–214